SDSS Standard Star Catalog for Stripe 82: the Dawn of Industrial 1% Optical Photometry

Željko Ivezić[1], J. Allyn Smith[2], Gajus Miknaitis[2], Huan Lin[2], Douglas Tucker[2], Robert H. Lupton[3], James E. Gunn[3], Gillian R. Knapp[3], Michael A. Strauss[3], Jon Holtzman[4], Steve Kent[2], Brian Yanny[2], David Schlegel[5], Douglas Finkbeiner[3], Nikhil Padmanabhan[6], Constance M. Rockosi[7], Mario Jurić[3], Nicholas Bond[3], Brian Lee[5], Sebastian Jester, Hugh Harris, Heather Morrison, Paul Harding, ...

ABSTRACT

We describe a standard star catalog constructed using multiple SDSS photometric observations (at least four, with a median of 10, per band) in the SDSS *ugriz* system. The catalog includes about 700,000 candidate standard stars from the equatorial stripe 82 ($|\mathrm{Dec}| < 1.266$ deg) in the RA range 20h 34' to 4h 00', and with the corresponding Johnson V band magnitudes in the range 14–21. The distributions of measurements for individual sources demonstrate that photometric pipeline correctly estimates random photometric errors, which are below 0.01 mag for stars brighter than (19.5, 20.5, 20.5, 20, 18.5) in *ugriz*, respectively (about twice as good as for individual SDSS runs). Several independent tests of the internal consistency suggest that the spatial variation of photometric zeropoints is not larger than ∼0.01 mag. In addition to being the largest available dataset with optical photometry internally consistent at the ∼1% level, this catalog effectively defines the SDSS photometric system. We illustrate several use cases for this catalog, including calibration of highly non-photometric data (up to 6 magnitudes of cloud extinction) and robust selection of stars with peculiar colors. In particular, we show that photometric

[1]University of Washington, Dept. of Astronomy, Box 351580, Seattle, WA 98195

[2]Fermi National Accelerator Laboratory, P.O. Box 500, Batavia, IL 60510

[3]Princeton University Observatory, Princeton, NJ 08544

[4]NMSU

[5]Lawrence Berkeley National Laboratory, One Cyclotron Road, MS 50R5032, Berkeley, CA, 94720

[6]Princeton University, Dept. of Physics, Princeton, NJ 08544

[7]University of California–Santa Cruz, 1156 High St., Santa Cruz, CA 95060

zeropoints for SDSS observing runs can be calibrated within nominal uncertainty of 2% even for data obtained through 1 mag thick clouds, and demonstrate the existence of He and H white dwarf sequences using photometric data alone. Based on the properties of this catalog, we conclude that upcoming large-scale optical surveys such as LSST should be capable of delivering robust 1% photometry for billions of sources.

1. Introduction

Astronomical photometric data are usually calibrated using sets of standard stars for which brightness is known from previous work. The most notable modern optical standard star catalogs are Landolt standards (Landolt 1992) and Stetson standards (Stetson 2000, 2005). Both are reported on the Johnson-Kron-Cousins system. The Landolt catalog provides ∼1-2% accurate magnitudes in the $UBVRI$ bands for ∼500 stars in the V magnitude range 11.5–16. Stetson has extended Landolt's work to fainter magnitudes, and provided the community with ∼1-2% accurate magnitudes in the $BVRI$ bands for ∼15,000 stars in the magnitude range $V \lesssim 20$. Most stars from both sets are distributed along the Celestial Equator, which facilitates their use from both hemispheres.

The data obtained by the Sloan Digital Sky Survey (SDSS) can be used to extend the work by Landolt and Stetson to even fainter levels, and to increase the number of standard stars. In addition, SDSS has designed its own photometric system ($ugriz$, Fukugita et al. 1996) which is now in use at a large number of observatories worldwide. This widespread use of the $ugriz$ photometric system motivates the construction of a large standard star catalog with ∼1% accuracy. Fortuitously, SDSS has obtained many scans in the so-called Stripe 82 region, defined by $|\mathrm{Dec}| < 1.266$ deg and RA approximately in the range 20h – 4h. These repeated observations can be averaged to produce more accurate photometry than the nominal 2% single-scan accuracy. Additional motivation for the analysis of repeated scans and their impact on the photometric accuracy is brought by the upcoming large-scale optical surveys such as Pan-STARRS (Kaiser 2002) and LSST (Tyson 2002). For example, LSST science requirements document calls for a photometric system that is internally consistent across the sky at the 1% level. The SDSS Stripe 82 repeated scans can be used to gauge the plausibility of delivering such a system.

We describe the construction and testing of a standard star catalog in §2, and illustrate its several use cases in §3. We discuss our results in §4.

2. The Construction of SDSS Stripe 82 Standard Star Catalog

2.1. Overview of SDSS imaging data

SDSS is providing homogeneous and deep ($r < 22.5$) photometry in five pass-bands (u, g, r, i, and z, Fukugita et al. 1996; Gunn et al. 1998; Smith et al. 2002; Hogg et al. 2002) accurate to 0.02 mag (root-mean-square scatter, hereafter rms, for sources not limited by photon statistics, Ivezić et al. 2003; and with a zeropoint uncertainty of ∼0.02, Ivezić et al. 2004a). The survey sky coverage of ∼10,000 deg^2 in the Northern Galactic Cap, and ~ 300 deg^2 in the Southern Galactic Hemisphere, will result in photometric measurements for well over 100 million stars and a similar number of galaxies[8]. Astrometric positions are accurate to better than 0.1 arcsec per coordinate (rms) for sources with $r < 20.5^m$ (Pier et al. 2003), and the morphological information from the images allows reliable star-galaxy separation to $r \sim 21.5^m$ (Lupton et al. 2002).

Data from the imaging camera (thirty photometric, twelve astrometric, and two focus CCDs, Gunn et al. 1998) are collected in the drift scan mode. The images that correspond to the same sky location in each of the five photometric bandpasses (these five images are collected over ∼5 minutes, with 54 sec per individual exposure) are grouped together for processing as a field. A field is defined as a 36 seconds (1361 pixels, or 9 arcmin) long stretch of drift-scanning data (for more details please see Stoughton et al. 2002). Each of the six scanlines (called together a strip) is 13 arcmin wide. The twelve interleaved scanlines (or two strips) are called a stripe (∼2.5 deg wide).

2.2. The Photometric Calibration of SDSS Imaging Data

SDSS 2.5m imaging data are photometrically calibrated using a network of calibration stars obtained in 1520 41.5×41.5 arcmin^2 transfer fields, called secondary patches. These patches are positioned throughout the survey area and are calibrated using a primary standard star network of 158 stars distributed around the Northern sky (Smith et al. 2002). The primary standard star network is tied to an absolute flux system by the single F0 subdwarf star BD+17°4708, whose absolute fluxes in SDSS filters are taken from Fukugita et al. (1996). The secondary patches are grouped into sets of four, and are observed by the Photometric Telescope in parallel with observations of the primary standards. Each set spans all 12 scan lines of a survey stripe along the width of the stripe, and the sets are

---

[8]The recent Data Release 5 lists photometric data for 215 million unique objects observed in 8000 deg^2 of sky, please see http://www.sdss.org/dr5/.

spaced along the length of a stripe at roughly 15 degree intervals, which corresponds to about an hour of scanning at the sidereal rate.

SDSS 2.5m magnitudes are reported on the "natural system" of the 2.5m telescope defined by the photon-weighted effective wavelengths of each combination of SDSS filter, CCD response, telescope transmission, and atmospheric transmission at a reference airmass of 1.3 as measured at APO[9]. The magnitudes are referred to as the *ugriz* system (which is different from the "primed" system, $u'g'r'i'z'$, that is defined by the Photometric Telescope[10], hereafter PT). The reported magnitudes[11] are corrected for the atmospheric extinction (using simultaneous observations of standard stars by the PT) and thus correspond to measurements at the top of the atmosphere[12] (except for the fact that the atmosphere has an impact on the wavelength dependence of the photometric system response). The magnitudes are reported on the AB system (Oke & Gunn 1983) defined such that an object with a specific flux of F_ν=3631 Jy has $m = 0$ (i.e. an object with F_ν=const. has an AB magnitude equal to the Johnson V magnitude at all wavelengths). In summary, given a specific flux of an object *at the top* of the atmosphere, $F_\nu(\lambda)$, the reported SDSS 2.5m magnitudes correspond to (modulo random and systematic errors, which will be discussed later)

$$m = -2.5\log_{10}\left(\frac{F_o}{3631\,\mathrm{Jy}}\right), \tag{1}$$

where

$$F_o = \int F_\nu(\lambda)\phi(\lambda)d\lambda. \tag{2}$$

Here, $\phi(\lambda)$ is the normalized system response

$$\phi(\lambda) = \frac{\lambda^{-1}S(\lambda)}{\int \lambda^{-1}S(\lambda)d\lambda}, \tag{3}$$

with the overall atmosphere+system throughput, $S(\lambda)$, available from the website given above (for a figure showing $\phi(\lambda)$ for the *ugriz* system see Smolčić et al. 2006).

---

[9]Transmission curves for the SDSS 2.5m photometric system are available at http://www.sdss.org/dr4/instruments/imager/.

[10]For subtle effects that led to this distinction, please see http://www.sdss.org/dr4/algorithms/fluxcal.html.

[11]SDSS uses a modified magnitude system (Lupton, Szalay & Gunn 1999), which is virtually identical to the standard astronomical Pogson magnitude system at high signal-to-noise ratios relevant here.

[12]It is noteworthy that the same atmospheric extinction correction is applied irrespective of the source color; although this may result in systematic errors, they are probably smaller than 1%.

The quality of SDSS photometry stands out among available large-area optical sky surveys (Ivezić et al. 2003a, 2004a; Sesar et al. 2006). Nevertheless, the achieved accuracy is occasionally worse than the nominal 0.02 mag (root-mean-square scatter for sources not limited by photon statistics). Typical causes of substandard photometry include an incorrectly modeled PSF (usually due to fast variations of atmospheric seeing, or lack of a sufficient number of the isolated bright stars needed for modeling), unrecognized changes in atmospheric transparency, errors in photometric zeropoint calibration, effects of crowded fields at low Galactic latitudes, undersampled PSF in excellent seeing conditions ($\lesssim$ 0.8 arcsec; the pixel size is 0.4 arcsec), incorrect flatfield, or bias vectors, scattered light correction, etc. Such effects can conspire to increase the photometric errors to levels as high as 0.05 mag (with a frequency, at that error level, of rougly one field per thousand).

2.3. The Choice of Cataloged Magnitudes

SDSS photometric pipeline (*photo*, Lupton et al. 2002) measures several types of magnitudes. For unresolved sources, the list includes aperture magnitudes, PSF (point spread function) magnitudes, and model magnitudes. Here we briefly describe each type of magnitude (for more details see Stoughton et al. 2002, and the SDSS website) and justify the choice of PSF magnitudes for catalog construction.

2.3.1. Aperture magnitudes

Aperture magnitudes are based on the flux contained within the aperture with a radius of 7.43 arcsec. While the most robust flux estimate at the bright end, these magnitudes do not have good noise properties at the faint end where the sky noise dominates (e.g. for a given maximum photometric error, say 0.1 mag, PSF magnitudes reach 1–1.5 mag fainter flux level). In order to improve the depth of the standard star catalog, we opt not to use aperture magnitudes, except for the quality tests at the bright end.

2.3.2. Point spread function magnitudes

The point spread function (PSF) flux is computed using the PSF as a weighting function. While this flux is optimal for faint point sources (in particular, it is vastly superior to aperture photometry at the faint end), it is also sensitive to inaccurate PSF modeling, which attempts to capture the complex PSF behavior. Even in the absence of atmospheric inhomogeneities, the SDSS telescope delivers images whose FWHMs vary by up to 15% from one side of a CCD to the other; the worst effects are seen in the chips farthest from the optical axis. Moreover, since the atmospheric seeing varies with time, the delivered image quality is a complex two-dimensional function even on the scale of a single frame. Without an accurate model, the PSF photometry would have errors up to 0.10-0.15 mag. The description of the point-spread function is also critical for star-galaxy separation and for unbiased measures of the shapes of nonstellar objects.

The SDSS imaging PSF is modeled heuristically in each band using a Karhunen-Loeve (K-L) transform (Lupton et al. 2002). Using stars brighter than roughly 20$^{\rm th}$ magnitude, the PSF from a series of five frames is expanded into eigenimages and the first three terms are retained. The variation of these coefficients is then fit up to a second order polynomial in each chip coordinate. The failure of this KL expansion, typically due to insufficient number of stars, or exceedingly complex PSF, results in occassional problems with PSF photometry.

2.3.3. Model magnitudes

Just as the PSF magnitudes are optimal measures of the fluxes of stars, the optimal measure of the flux of a galaxy would use a matched galaxy model. With this in mind, the photometric pipeline fits two models to the two-dimensional image of each object in each band: a pure deVaucouleurs profile and a pure exponential profile[13]. Because the models are convolved with a double-Gaussian fit to the PSF, the seeing effects are accounted for. Aperture corrections are applied to make these model magnitudes equal the PSF magnitudes in the case of an unresolved object. Probably because these model fits have more degrees of freedom than the PSF modeling, the incidence of large photometric errors for unresolved sources is somewhat smaller than for the PSF magnitudes.

2.3.4. The choice of magnitudes for the standard star catalog

The comparison between aperture, PSF and model magnitudes is done automatically for every SDSS observing run (*runQA* pipeline, Ivezić et al. 2004a). Analysis of over 200 runs indicate that model magnitudes are more robust than PSF magnitudes: while the former fail at the 0.05 mag level (relative to aperture magnitudes) about once per thousand

[13]For more details see http://www.sdss.org/dr4/algorithms/photometry.html

fields, the failure frequency is about three times higher[14] for PSF magnitudes. On the other hand, the analysis of repeated scans indicates that estimates of photometric errors by photometric pipeline are more accurate for PSF magnitudes (agreeing at the 10% level with the measured values) than for model magnitudes (discrepant from the measured values by typically 30-50%). Because the rejection of likely variable sources, which relies on accurate photometric error estimates, is an important step in the construction of the standard star catalog (see below), we choose to use PSF magnitudes to construct the catalog.

2.4. The Catalog Construction

Using 58 SDSS-I runs from stripe 82 (approximately 20h $<$ RA $<$ 04h and $|\mathrm{Dec}| <$ 1.266) obtained in mostly photometric conditions (as indicated by the calibration residuals, infrared cloud camera[15], and tests performed by *runQA* pipeline), candidate standard stars from each run are selected by requiring

1. that objects are classified as STAR,
2. that they have quoted photometric errors (as computed by the photometric pipeline) smaller than 0.05 mag in at least one band, and
3. that processing flags BRIGHT, SATUR, BLENDED, EDGE are not set[16].

These requirements select unique unsaturated sources with sufficiently high signal-to-noise per single observation to approach the final photometric errors of 0.02 mag or smaller.

After positionally clustering (within 1 arcsec) all detections of a single star, various photometric statistics such as mean, median, root-mean-square scatter, number of observations, and χ^2 per degree of freedom (χ^2_{pdf}) are computed in each band. This initial catalog of multi-epoch observations includes 924,266 stars with at least 4 observations in each of the g, r and i bands. The median number of observations per star and band is 10, and the total number of photometric measurements is $\sim$40 million.

The distributions of the median magnitudes, their photometric errors, χ^2_{pdf} and the number of observations for a subset of these stars are shown in Figure 1. Note that the

---

[14]This result is also explicitly tested in §3.

[15]For more details about the camera see http://hoggpt.apo.nmsu.edu/irsc/irsc_doc/.

[16]For more details about processing flags see Stoughton et al. (2002) and http://www.sdss.org/dr4/products/catalogs/flags.html.

random errors in the median magnitude (computed as 0.928*IQR/$\sqrt{N-1}$, where IQR is the 25%–75% interquartile range of the individual measurement distribution and N is the number of measurements; for a Gaussian distribution these errors would be 25% larger than the error of the mean, Lupton 1993) are below 0.01 mag at the bright end. These errors are reliably computed by photometric pipeline, as indicated by the χ^2_{pdf} distributions. The distribution of these stars in color-magnitude and color-color diagrams is shown in Figure 2.

Adopted candidate standard stars must have at least 4 observations and, to avoid variable sources, χ^2_{pdf} less than 3 in the gri bands (the same requirements are later applied in the u and z bands when using the catalog for calibration, for more details see below). We also limit the RA range to 20h 34' < RA < 04h 00', which provides a simple areal definition (together with |Dec| <1.266 deg) while excluding only a negligible fraction of stars. These requirements result in a catalog with 681,262 stars. Of those, 638,671 have the random error for the median magnitude in the r band smaller than 0.01 mag (664,288 if the error for the mean is used instead), and 499,188 in all the three (gri) bands. Subsets of 198,993 and 531,192 stars satisfy these requirements in the ugri and griz bands, and 198,182 stars in all five bands. Of the latter, 131,014 stars have the random error for the median magnitude smaller than 0.01 mag in all five bands. The distribution of candidate standard stars, that satisfy the above selection criteria in all five bands, in color-magnitude and color-color diagrams is shown in Figure 3.

For completeness, the distribution of sources that were rejected as variable in color-magnitude and color-color diagrams is shown in Figure 4. As evident from a comparison with Figure 3, the distribution of variable sources in color-color diagrams is markedly different from that of non-variable sources. It is especially striking how low-redshift ($z < 2.2$) quasars are easily detected by their variability (for more details see Ivezić et al. 2004b). However, it is fairly certain that not all variable sources are recognized as such because of the limited number of repeated observations (∼10). For example, an eclipsing binary with much shorter eclipse duration than the orbital period could easily escape detection.

The sky density of all the sources and those selected as candidate standard stars are shown in Figure 5. Note that at high galactic latitudes ($|b| \sim 60$) the fraction of non-variable point sources is ∼80%.

2.5. The Tests of Catalog Quality and Flatfield Corrections

Figure 1 demonstrates that random photometric errors behave as expected. However, the measurements are also subject to systematic calibration errors such as the spatial dependence of the internal zeropoints, and the overall deviations of the internal zeropoints from AB magnitude scale. Formally, the true AB magnitude of an object, m_{true}, can be expressed as

$$m_{true} = m_{cat} + \delta_m(\mathrm{RA}, \mathrm{Dec}) + \Delta_m, \tag{4}$$

where m_{cat} is the cataloged magnitude, $\delta_m(\mathrm{RA}, \mathrm{Dec})$ describes the spatial variation of the internal zeropoint error around Δ_m (i.e. the average of δ_m over the cataloged area is 0 by construction), and Δ_m is the overall (spatially independent) deviation of the internal SDSS system from a perfect AB system (i.e. the five values Δ_m are equal for all the cataloged objects). Here we assume that any systematic errors due to different source spectral energy distributions can be accounted for separately, which is true at the 1% accuracy level relevant here.

The spatial variation of the internal zeropoint error can be separated into *color* errors, relative to a fiducial band, say r, and an overall "gray" error (e.g. due to unrecognized temporal changes in atmospheric transparency)

$$\delta_m(\mathrm{RA}, \mathrm{Dec}) = \delta_r(\mathrm{RA}, \mathrm{Dec}) + \delta_{mr}(\mathrm{RA}, \mathrm{Dec}), \tag{5}$$

with $\delta_{mr} = \delta_m - \delta_r$. Below we discuss methods for estimating both the "gray" error $\delta_r(\mathrm{RA}, \mathrm{Dec})$ and the color errors $\delta_{mr}(\mathrm{RA}, \mathrm{Dec})$.

The deviation of the internal SDSS system from a perfect AB system, Δ_m, can also be expressed relative to the fiducial r band

$$\Delta_m = \Delta_r + \Delta_{mr}. \tag{6}$$

The motivation for this separation is twofold. First, Δ_{mr} can be constrained by considering the colors (spectral energy distributions) of objects, independently from the overall flux scale. Second, it is hard to find a science result that crucially depends on knowing the "gray scale" offset, Δ_r, at the 1-2% level. On the other hand, knowing "the band-to-band" offsets, Δ_{mr}, with such an accuracy is important for many applications (photometric redshifts of galaxies, type Ia supernovae cosmology, testing of stellar and galaxy models, etc.).

Using SDSS spectra of hot white dwarfs, Eisenstein et al. (2006) constrained Δ_{mr} to be −0.04, −0.01, 0.015 and 0.03 mag for $m = ugiz$ with an accuracy of ∼0.01 mag. The overall "gray" flux scale calibration error, Δ_r, is determined by the accuracy of the absolute flux calibration of fundamental standard BD+17°4708, the accuracy of tying the primary standard star network to BD+17°4708, the accuracy of transfering the primary standard star network to the secondary standard star network, and the accuracy of the calibration of the survey imaging data using the secondary standard star network. Given these numerous sources of error, it seems unlikely that $\Delta_r < 0.02$ mag. On the other hand, formal analysis of all the error contributions suggests that Δ_r does not exceed 0.05 mag. Note, however, that all these uncertainties in the definition and transfer of the standard star network become moot if one accepts that

1. Δ_r does not need to be known exquisitely well. Even if it does, this is just *a single number* that modifies the cataloged photometry for all the sources and all the bands in the same fashion.

2. Errors in the determination of Δ_{mr} are indeed of the order 0.01 mag.

3. $\delta_m(\mathrm{RA}, \mathrm{Dec})$ can be constrained, or corrected for, at the 0.01 mag level.

In other words, the band-to-band calibration is fixed by adopting Δ_{mr}, $\delta_m(\mathrm{RA}, \mathrm{Dec})$ guarantees internal consistency, and the only remaining relatively free parameter is Δ_r.

We now proceed to describe methods for constraining $\delta_m(\mathrm{RA}, \mathrm{Dec})$. The region covered by the SDSS Stripe 82 is a very elongated rectangle with the 50:1 aspect ratio, and with the long side parallel to the Celestial Equator. Because of this large aspect ratio, and because different effects contribute to the RA and Dec dependences of δ_m, we assume that it can be expressed as a sum of two independent functions of either RA or Dec,

$$\delta_m(\mathrm{RA}, \mathrm{Dec}) = \delta_m^{ff}(\mathrm{Dec}) + \delta_m^{ext}(\mathrm{RA}), \tag{7}$$

with $< \delta_m^{ff}(\mathrm{Dec}) >_{\mathrm{RA}} = 0$ and $< \delta_m^{ext}(\mathrm{RA}) >_{\mathrm{Dec}} = 0$, where $< \delta >_x$ denotes the average of δ over direction x.

The first term, $\delta_m^{ff}(\mathrm{Dec})$, is dominated by the errors in flatfield vectors (for drift scanning, flatfield corrections are one-dimensional). The flatfield determination for SDSS was difficult[17] and it is likely that there are systematic errors in the stellar photometry at the 0.01 mag level in the *griz* bands and the 0.02 mag level in the u band (perhaps somewhat larger for the u chips at the edge of the imaging camera). Since these systematic errors do *not* cancel when averaging many observing runs (because most stars are always observed by the same chip and fall on roughly the same position within the chip), δ_{mr}^{ff} could

[17]For details please see http://www.sdss.org/dr4/algorithms/flatfield.html.

deviate from 0 by as much as $\sim 0.01 - 0.02$ mag on spatial scales much smaller than the chip width (13 arcmin).

The second term, δ_{mr}^{ext}(RA), is dominated by unrecognized fast variations of atmospheric extinction (e.g. due to cirrus) because for each observing run only a single zeropoint per CCD is determined (slow change of atmospheric extinction due to varying airmass is accounted for, and the hardware is stable at the 1% level). While such variations are uncorrelated for different runs, it is possible that they are not fully avoided by the averaging procedure at the 1% level.

We use three methods based on SDSS data to constrain δ_m^{ff}(Dec) and δ_{mr}^{ext}(RA): a direct comparison with secondary standard star network, a method based on stellar colors, and a method based on photometric redshift relation for galaxies. Each of these methods has its advantages and disadvantages. In addition, we compare the SDSS photometry to an independent set of standards provided by Stetson (2000, 2005).

2.5.1. The comparison with secondary standard star network

A direct comparison with secondary standard star network (hereafter PT comparison) could be considered as *a priori* the best method. However, it is quite possible that the secondary standard star network may induce a spatial variation of the photometric zeropoints at the 0.01 mag level. In addition, there are not enough stars to constrain δ_m^{ff}(Dec) with a sufficient spatial resolution (say, at least ∼100 pixels, or ∼0.01 deg). For example, there are ∼20,000 stars from Stripe 82 that are not saturated in the *gri* bands in the 2.5m scans, and have PT errors smaller than 0.03 mag (∼8,000 stars are available in the z band, and only ∼3,000 in the u band). If binned in Dec direction every 0.01 deg (250 90-pixels wide bins), δ_m^{ff} in each bin can be constrained to about ∼0.005 mag (0.01 mag in the u band). This is barely sufficient in the *gri* bands, and cannot provide satisfactory constraints on the flatfielding errors in the u band (where unfortunately these errors are the largest). Similarly, δ_m^{ext}(RA) could be constrained in 0.5 deg wide bins with a similar accuracy, but the problem is that the secondary standard stars are not uniformly distributed. For these reasons, we combine the PT comparison with the stellar locus method, described next, when determining flatfield corrections, as detailed further below.

2.5.2. The stellar locus method

The stellar distribution in the color-color space is remarkably uniform at faint flux levels probed by SDSS and at high galactic latitudes[18] ($|b| > 30$), as discussed in detail by Ivezić et al. (2004a). Systematic photometric errors manifest themselves as shifts in the position of the stellar locus (except for an overall gray error) that can be tracked using the four principal colors ($swxy$) defined in Ivezić et al. (2004a). These colors measure the distance from the center of the locus in various two-dimensional projections of the four-dimensional stellar color distributions (of course, the measurements must be corrected for the effects of interstellar dust extinction, we use maps provided by Schlegel, Finkbeiner & Davis 1998, hereafter SFD98). The properties of two of these colors are illustrated in Figure 6.

The fact that the median principal colors are close to 0 shows that the averaging procedure did not induce any shifts in zeropoints compared to the average of 291 runs discussed by Ivezić et al. (2004a). The same conclusion is reached by comparing the averaged photometry with the secondary standard star network: the median photometric residuals at the so-called crossing colors[19] are 4, 6, 3, 2 and 2 millimag in the $ugriz$ bands, respectively (using 0.04 mag wide bins around crossing colors). Yet another test is a direct comparison of averaged photometry with single-epoch photometry. Using the SDSS Data Release 5 photometry, we find that the largest median deviation between the two sets is 2 millimag in the u band.

It is noteworthy that the widths of the principal color distributions (i.e. the thickness of the stellar locus) constructed with averaged photometry are much smaller than when using single-epoch data (see the bottom four panels in Figure 6). Indeed, all four principal color distributions are "resolved" using this high quality photometry (see Table 1). This decrease of the width is in agreement with the above discussion of random photometric errors.

Because the widths of principal color distributions are so small, principal colors can be used to efficiently track local calibration problems using a small number of stars, which allows a high spatial resolution (i.e. deviations of the median values of principal colors in appropriately defined bins indicate zeropoint errors). For example, in a bin with 100 stars, the median s color can be determined with an accuracy of ~0.002 mag. Such a shift would

---

[18] At low galactic latitudes several effects, discussed below, prevent the use of this method for calibration purposes.

[19] For details see http://www.sdss.org/dr4/algorithms/jeg_photometric_eq_dr1.html

be induced by a zeropoint error in the u band of 0.008 mag (assuming that the g and r bands are perfectly calibrated). Typically, there are several hundred stars per bin, with bins 0.01 deg wide in Dec direction and 1 deg in RA direction. While this procedure can only constrain δ_{mr}, this is an additional method, independent of calibration star networks, that can measure δ_{mr} with a very high spatial resolution.

2.5.3. The flatfield corrections

The main advantage of the stellar locus method is that it can constrain δ_{mr} with a high spatial resolution. However, it is insensitive to gray errors, parametrized by δ_r (e.g. an overall gradient of photometric zeropoints in Dec direction equal in all five bands would have no effect on stellar colors). On the other hand, the PT comparison can constrain δ_r, but it does not provide enough spatial resolution to derive flatfield corrections, especially in the u and z bands. Therefore, we combine these two methods to derive flatfield corrections δ_m^{ff}(Dec).

The median differences between the averaged 2.5m photometry and PT photometry for secondary standard stars in the gri bands are shown in Figure 7. The median differences are computed for 0.01 deg wide bins, and then smoothed by a triangular filter (y_i is replaced by $0.25 * (y_{i-1} + 2y_i + y_{i+1})$). All three bands display similar behavior of residuals, and imply about 2% peak-to-peak variation between the center and edges on each CCD (resulting in about 0.006 mag rms contribution to the overall errors), as well as an overall 2% tilt. These systematic errors may be due to imperfect flatfield vectors used to reduce the data, or to incorrectly determined scattered light correction (the two are somewhat coupled in the data reduction procedures). At the face value, these residuals could be used to correct the averaged 2.5m photometry in each band separately. However, a test based on stellar locus (compare the top and bottom panels in Figure 7) suggests that the differences in photometric residuals between the three bands are dominated by noise, and that such corrections introduce unnecessary noise in stellar colors (parametrized by δ_{mr}). On the other hand, the 2.5m vs. PT residuals do contain information about "gray" errors that cannot be determined using stellar locus. Hence, we take the *mean* value of the 2.5m vs. PT residuals in the gri bands to represent the δ_r flatfield correction, and apply it to the averaged 2.5m photometry in the r band. The applied correction is shown in Figure 8 and has an rms scatter of 7 millimag (for 250 bins), with the largest correction of <0.02 mag.

In the second step, we use the stellar locus to derive the δ_{mr} corrections in each band ($ugiz$). The derivation of these corrections is essentially identical to the procedure described by Ivezić et al. (2004a). Also, together with a PT-based δ_r correction, this is essentially the same method as used to derive flatfield corrections for the whole SDSS survey[20]. In particular, we used here the same closure relation (stellar locus method gives four equations for five unknowns), that is based on averaged 2.5m vs. PT residuals in the *gri* bands. The resulting flatfield corrections, δ_{mr}, in the *ugiz* bands are shown in Figure 8.

It is noteworthy that the u band correction is expected to have the largest noise, which is consistent with the observed behavior. It is thus likely that some of the variation with high spatial frequency (on scale of ∼0.1 deg) is not real. On the other hand, it could be argued that systematic errors could actually be much larger on even smaller spatial scales, but get averaged out in 90 pixel wide bins. However, in addition to not having a reason to believe in such high spatial frequency effects (e.g. the sky background does not show any evidence for them), the mean χ^2 per degree of freedom stays ∼1 even when the bin size is decreased by a factor of 4 (i.e. no additional scatter, except the expected statistical noise, is observed).

Note that we could have applied the PT-based δ_r flatfield correction in other bands, too. The only difference would be a change in derived δ_{mr} corrections, but the final corrected photometry would be the same. Similarly, we could have first derived δ_{mr} using the stellar locus method and $\delta_r = 0$ assumption, and then applied a PT-based δ_r flatfield correction in all five bands.

Last but not least, it is important to emphasize that these corrections are not setting photometric zeropoints, but only correcting for variations in response across each CCD. As discussed above, the AB photometric zeropoints, relative to the fiducial r band, *are effectively set by adopting* Δ_{mr} from Eisenstein et al. (2006). The overall flux scale, and its error parametrized by Δ_r is tied to BD+17°4708, through a series of calibration steps. However, we emphasize that Δ_r is just *a single number*, applicable in a trivial manner to all the SDSS photometry.

2.5.4. The tests of the final catalog quality

As a first test, we simply recompute the PT vs. 2.5m residuals and stellar locus positions using the final catalog (internally called v2.4), and bin them in Dec direction. The observed scatter is consistent with statistical noise, as expected. A more interesting test is obtained by binning in RA direction.

At least in principle, the same methods used to derive δ_m^{ff}(Dec) could be used to derive

[20]For details see http://www.sdss.org/dr4/algorithms/flatfield.html.

δ_m^{ext}(RA). However, in practice this is not possible for at least two reasons: first, the RA distribution of secondary standard stars is not as uniform as their Dec distribution, and second, the assumption of the constancy of the stellar locus in color space is invalid along the "long" scan direction (120 degrees long, and approaching low galactic latitudes and regions of high interstellar dust extinction). For these reasons, we only use PT comparison and stellar locus methods to estimate the level of internal zeropoint variations with RA, and do *not* correct the data. We also use another method, based on galaxy colors, as an independent test of catalog integrity.

Figure 9 shows the median principal colors as a function of RA. As evident, the principal colors are close to 0 for $-25 < \mathrm{RA} < 40$, but outside this range deviate significantly from 0. This does not necessarily indicate problems with photometric calibration, because the stellar locus method is expected to fail at low galactic latitudes due to several reasons. First, the metallicity increases and this change may affect the s and w colors. Second, at low latitudes red dwarfs are not behind the entire dust screen measured by the SFD98 maps (see section in Jurić et al. 2006 for a discussion of this point), and thus the x color will be biased blue (i.e. the colors are over-corrected for the ISM reddening). And third, at low latitudes the dust column increases fast (see Figure 10) and even small errors in the *assumed* wavelength dependence of the dust extinction, or the extinction itself as given by the SFD98 maps, will have noticeable effects on principal colors. For these reasons, it seems plausible that the deviations seen in Figure 9 are *not* dominated by zeropoint errors.

This conclusion is supported by the direct comparison of the averaged and PT photometry (Figure 10). For example, the largest median photometric residual between the averaged catalog and PT observations in the u band is $\sim$0.02 mag (see Table 3), which is much smaller than 0.1 mag discrepancy implied by the stellar locus method. In addition, we further test this conclusion using galaxy colors, described in the next section.

Table 3 shows that the rms scatter of median photometric residuals (evaluated in 2 deg wide bins in RA directon) between the averaged catalog and PT observations is $<$0.01 mag in all five bands. It is worth emphasizing that some of that scatter must come from the PT data itself, and thus the true scatter of photometric zeropoints in the averaged catalog is even smaller than that listed in Table 3. In addition, Table 3 shows that the averaged catalog and PT measurements are on the same system to within a few millimags (using the recommended photometric transformations listed at the SDSS website, see Section 2.2).

2.5.5. The tests of catalog quality based on galaxy colors

The color distribution of galaxies is bimodal (Strateva et al. 2001, Shimasaku et al. 2001, Baldry et al. 2003). Red galaxies have especially tight color-redshift relation, with rms of 0.12 mag for the $u-g$ color, 0.05 mag for the $g-r$, and 0.03 mag for the $r-i$ and $i-z$ colors. Deviations from the mean relations can thus be used to track local calibration problems. Of course, since this is a color-based method, it can only constrain δ_{mr}, and, because red galaxies are faint in the u band, cannot achieve high spatial resolution in this band. Nevertheless, it is a useful addition to the stellar locus method because it is independent of the Milky Way structure and secondary star network (although it is sensitive to errors in the ISM dust extinction correction).

We select 19,422 red galaxies from the redshift range 0.02–0.36 by the condition

$$0 < (g-r) - 0.6 - 2.75 \times \mathrm{redshift} < 0.3, \tag{8}$$

and determine their median colors as a function of redshift using 0.01 wide redshift bins (we use model magnitudes in this analysis). The residuals from the median color–redshift relation are then binned by Dec to constrain δ_m^{ff} and by RA to constrain δ_m^{ext}. The rms for color residuals and the widths of distributions of residuals normalized by statistical noise are listed in Table 4.

The residuals binned in Dec direction are generally small and consistent with statistical noise, except for the $i-z$ color. Although the rms is small (6 millimag, i.e. smaller than random photometric errors), it is 2.6 larger than expected noise, and color residuals show systematic variation with Dec, with an amplitude of ∼0.010-0.015 mag (see the top panel in Figure 11. It is not clear what is the cause of this (small) effect, but it doesn't appear to be a problem with the photometric zeropoints because the stellar colors do not show such variation (by construction, as they were used to constrain the flatfield corrections). The implied variation of the $i-z$ color measured using stellar colors is about three times smaller than the deviation displayed by galaxies. It is noteworthy that the latter seems to have structure on the scale of ∼0.2 deg (the CCD width), and thus could be related to scattered light effects[21].

The results for RA binning are shown in Figure 12, where we compare all three methods. The rms for implied color errors (with 2 deg wide bins) is 0.006 mag for the $r-i$

[21]It is fair to ask whether the applied flatfield corrections were actually appropriate for galaxies. They are since the $i-z$ color residuals for galaxies without flatfield corrections are about 50% larger than those shown in the top panel in Figure 11.

and $i-z$ colors, 0.012 mag for the $g-r$ color, and 0.018 mag for the $u-g$ color. The overall behavior of red galaxy color residuals agrees better with the PT method, than with color errors implied by the stellar locus method. In particular, the large errors outside the $-25 <$ RA < 40 range implied by the latter method are not consistent with red galaxy color residuals. On the other hand, both red galaxy colors and stellar locus seem to show a trend that the colors are *redder* around RA=-10 deg than around RA=40 deg. The amplitude of this effect varies from about 0.02 mag for the $g-r$ color to about 0.01 mag for the $i-z$ color, while the upper limit on such a slope implied by the PT comparison is <0.01 mag.

It is not clear what could be the cause of this discrepancy. The obvious culprit is the correction for interstellar dust extinction, but the implied deviation is too large to be explained by any plausible errors in the SFD98 maps. As shown in Figure 10, the median extinction in the r band for the $-10 <$ RA < 40 range is below 0.1 mag, and the resulting median correction for, e.g., the $g-r$ color is below 0.04 mag. Hence, to induce a 0.02 mag trend in the $g-r$ color, the SFD value for the r band extinction, A_r, would have to be in error by 0.05 mag (the difference between the values provided for RA=-10 deg and RA=40 deg). This implies relative errors for the SFD map in the range 50% (if A_r at RA=-10 deg is underestimated) to 100% (if A_r at RA=40 deg is overestimated), which seems unlikely (though not impossible).

We conclude that the PT comparison provides a good estimate of the remaining zeropoint errors in the catalog, as listed in Table 3, but caution that we do not understand the above systematic behavior of stellar and galaxy colors, and that we have no other internal constraint but PT for the possible gray errors. In the next Section, we discuss a comparison to an external dataset, that supports this conclusion.

2.5.6. An external test of catalog quality based on Stetson's standards

It is not easy to thoroughly test the quality of the Stripe 82 catalog using an external dataset because of its depth and the target accuracy of 1%. The only large dataset with sufficient overlap, depth and accuracy is that provided by Stetson (2000, 2005). For ∼1,200 stars in common (most have $V < 19.5$), Stetson's catalog lists photometry in the $BVRI$ bands. We synthesize the $BVRI$ photometry from SDSS $ugriz$ measurements using photometric transformations of the following form

$$m_{\rm Stetson} - \mu_{\rm SDSS} = A\,(g-i)^3 + B\,(g-i)^2 + C\,(g-i) + D, \tag{9}$$

where $m = (BVRI)$ and $\mu = (g, g, r, i)$, respectively, and the $g-i$ color is measured by SDSS (not corrected for the ISM reddening). Typically, such transformations are assumed to be linear in color, and use different colors for different (m, μ) pairs[22] (e.g. $g - r$ for $B - g$ and $V - g$, $r - i$ for $R - r$ and $i - z$ for $I - i$). It is not necessary to use different colors because the stellar color distribution is nearly one-parameter family (e.g. Ivezić et al. 2004a, Jurić et al. 2006) and any color constructed with the $griz$ bands could serve the purpose[23]. The chosen color $(g - i)$ has the best combination of the wavelength range and signal-to-noise ratio. We use the higher-order terms because at the 1-2% level there are easily detectable deviations from linearity (which do not go away for different color choices). The best-fit $ABCD$ coefficients for the transformation of SDSS $griz$ measurements to the $BVRI$ system[24] (Stetson's photometry is tied to the Landolt system) are listed in Table 5, as well as low-order statistics for the $m_{\rm Stetson} - \mu_{\rm SDSS}$ difference distribution. We find no trends as a function of magnitude at the < 0.005 mag level. We have also tested for the effects of metallicity on the adopted photometric relations. Stars at the blue tip of the stellar locus with $u - g < 1$ are predominantly low-metallicity stars (Bond et al. 2006, in prep.). The median residuals for $m_{\rm Stetson} - \mu_{\rm SDSS}$ colors (i.e. the difference between the measurements and the fit) are the same for $0.8 < u - g < 0.95$ and $1.0 < u - g < 1.1$ subsamples to within 5 millimag, or better (and close to 0, as listed in Table 5). Hence, the catalog presented here could also be used to calibrate the data to the BVRI system.

The $BVRI$ photometry from Stetson and that synthesized from SDSS agree at the level of 0.02 mag (rms scatter for the magnitude differences of individual stars; note that the systems are tied to each other to within a few millimags by transformations listed in Table 5). This scatter is consistent with the claimed accuracy of both catalogs (the magnitude differences normalized by the implied error bars are well described by Gaussians with widths in the range 0.7–0.8). This small scatter allows to test for the spatial variation of zeropoints between the two datasets, despite the relatively small number of stars in common.

Stars in common are found in well separated small patches that belong to the following four regions: **R1:** RA∼325, Dec<0; **R2:** RA∼15; **R3:** RA∼55; **R4:** RA∼325, Dec>0. We

---

[22]For various photometric transformations between the SDSS and other systems, see http://www.sdss.org/dr4/algorithms/sdssUBVRITransform.html.

[23]If for some reason only the $g - r$ or $r - i$ color should be used, the $g - i$ color for the main sequence stars can be synthesized using the parametrization of the stellar locus given by Jurić et al. (2006). Similarly, the $r - i$ color can be synthesized from the $i - z$ color using $r - i = -2.741x^3 + 2.655x^2 + 0.9282x + 0.109$, with $x = i - z$. However, the mean rms uncertainty of this $r - i$ color is as large as 0.09 mag.

[24]The same transformations can be radily used to transform measurements in the $BVRI$ system to the corresponding $griz$ values. Algebra can be greatly simplified by using the fact that the relationship between the $V - I$ and $g - i$ colors is linear at the 1% level: $V - I = 0.71(g - i) + 0.325$.

determine the zeropoint offsets between the SDSS and Stetson's photometry for each region separately, which gives us similar constraints for the gri zeropoint offsets to those based on PT data (as shown in the bottom panel in Figure 10). However, due to much smaller number of stars, there are only four points in each band. The implied zeropoint errors (which, of course, can be due to either SDSS or Stetson's dataset, or both) are listed in Table 6. For regions 1-3 the implied errors are only a few millimags (except for the $B - g$ color in region 1). The discrepancies are much larger for the three red colors in region 4. A comparison with the PT-based results shown in Figure 10, and color-based methods shown in Figure 12, suggest that these discrepancies are more likely due to zeropoint offsets in Stetson's photometry for this particular region, than to problems with SDSS photometry. We contacted P. Stetson who confirmed that his observing logs were consistent with this conclusion. We point out that only a small fraction of stars from Stetson's list are found in this region.

Given the results presented in this Section, we conclude that the rms for zeropoint errors in the SDSS Stripe 82 catalog is below 0.01 mag in all five bands.

3. The Utility of SDSS Stripe 82 Standard Star Catalog

As examples of the use of the standard star catalog, we discuss calibration of data obtained in non-photometric conditions, and a detailed and robust measurement of the stellar locus morphology.

3.1. Calibration of Non-photometric data

SDSS-II SNe survey aims to obtain data with a sufficient cadence to enable discovery of new type Ia supernovae. This requirement sometimes results in observations obtained through clouds with several magnitudes of extinction. In such highly non-photometric conditions the standard photometric calibration described in section 2.2 fails because the patches with standard stars are too sparsely distributed to be able to resolve fast variations in cloud extinction.

3.1.1. A method to track fast cloud extinction variations

Due to its high stellar density, the standard star catalog described in previous section can be used for calibration of data obtained in grossly non-photometric conditions. Typical number of calibration stars per one SDSS field (9x13 arcmin^2) at high galactic latitudes is 10-15 in the u band, 40-50 in the gri bands, and 30-40 in the z band. Based on tests of several such SDSS-II runs, it was found that the cloud extinction variations can be tracked with a sufficient temporal resolution ($\sim$3 sec) to obtain photometric zeropoint accuracy comparable to that characteristic for photometric nights (1-2% in the gri bands, and 2-3% in the u and z bands; Ivezić et al. 2004a).

The calibration is done in two steps. First, the implied zeropoints (whose variation is dominated by cloud extinction), zp, defined by

$$m_{calibrated} = -2.5 * \log(counts) + zp, \tag{10}$$

are median filtered using a window with 5 stars in order to avoid outliers. In the second step, zeropoints are evaluated for each 2048 pixel wide (cross-scan direction) and 100 pixel long (in-scan direction) image segment, hereafter called a calibration patch. That is, a calibration patch is a $\sim$5 arcmin^2 square rectangle with an aspect ratio 1:20, and the zeropoints are evaluated every 2.6 seconds of time (though note that the variations are smoothed out by the 54 sec long exposure time).

The patch is much narrower in the in-scan direction because tests have shown that zeropoint gradients across a field are much larger, by a factor 10-30, in this direction (see Figure 13). It is straightforward to understand why the zeropoint gradients are much larger in the scan direction. Consider three stars, star A, a star B that is, say, 25 arcmin (the column-to-column separation) away from the star A in the scan direction, and a star C that is 25 arcmin away from the star A in the cross-scan direction. Stars A and C are observed at the same time and the difference in their implied zeropoints measures the structure of cloud opacity on a 25 arcmin spatial scale. This is true irrespective of the cloud motion relative to the boresight. Here, the structure function of cloud opacity is defined as the rms width of the distribution of zeropoint differences evaluated for pairs of points separated by some distance.

On the other hand, stars A and B are observed at times that differ by 1.7 minutes. If the component of the cloud angular velocity on the sky relative to the boresight and parallel to the scanning direction is w deg/min, the zeropoint difference for stars A and B samples the cloud structure on spatial scales of 25 w/w_s arcmin, where w_s=0.25 deg/min is the sidereal scanning rate (here for simplicity we assumed $w >> w_s$, which is supported by the data). The observed behavior of zeropoints, such as that shown in Figure 13, implies wind velocity in the range[25] w=3-15 deg/min. Hence, drift scanning has an unfortunate

[25]This range is equivalent to angular speeds of up to a half of the Moon's diameter per second. The

property that the motion of an inhomogeneous extinction screen with a speed much larger than the sidereal scanning rate greatly magnifies the effective zeropoint variations in the scan direction.

The zeropoints for each calibration patch are computed by finding the smallest window centered on the patch that includes at least 3 stars, and adopting the median zp for these stars. This is certainly not the only, nor the best way to calibrate patches, but we found that it works well in practice. The zeropoint error is evaluated from the root-mean-square scatter of zp, divided by the square root of the number of stars. We discuss the performance of this method next.

3.1.2. Performance and Quality Tests

The top panel in Figure 14 summarizes the behavior of cloud extinction in the r band for an SDSS-II SN run (5646) obtained in strongly non-photometric conditions. Although the cloud extinction during the first 150 fields (corresponding to 1.5 hours of time) varies between 0 and $\sim$6 mag, it is possible to robustly calibrate these data. Figure 15 zooms in on a 2 minutes long stretch of the same data where the cloud extinction varies between 1 and 3 mag, with changes as fast as 0.03 mag/second. As shown in the figure (middle left panel), the residuals have the distribution width of only 0.07 mag. The middle right panels in Figures 14 and 15 demonstrate that most of this scatter is contributed by random photometric errors (i.e. errors in extracted source counts), rather than by calibration errors (large cloud extinction results in a smaller number of calibration stars, as well as in a lower SNR for those calibration stars that are detected). Even with such a large and fast varying cloud extinction, the zeropoint errors are smaller than 0.06 mag, with the median value of only 0.02 mag. Two examples from other runs, where the cloud extinction is more moderate, are shown in Figures 17 and 16.

The cloud extinction significantly decreased during the second half of run 5646. However, a detailed look (see Figure 18) reveals remaining cloud extinction at the 0.05 mag level that oscillates between 0 and 0.1 mag, with rms of $\sim$0.02 mag, on time scales of the order 1 minute (note that the true variations are somewhat smoothed out by the 54.1 second long integration time). As the bottom right panel in Figure 18 demonstrates, the median zeropoint error is only 0.004 mag (of course, this error does not include random and systematic photometric errors in the calibration star catalog, which are comparable).

---

plausibility of this wind velocity range was verified in extensive visual observations of the full Moon during frequent grossly non-photometric nights in Seattle.

These variations, with an rms of 0.02 mag, could be do to problems with psf magnitudes (c.f. Section 2.3). For this reason, we chose a run obtained in nominally photometric conditions (2662) and compare zeropoint variations obtained using aperture, psf and model magnitudes (see Figure 19). As discussed in Section 2.3, the aperture magnitudes are more robust than model and PSF magnitudes, but they are much noiser at the faint end. Hence, for grossly non-photometric nights with several magnitudes of cloud extinction either model or psf magnitudes are superior to aperture magnitudes. On the other hand, for studying low-level atmospheric transparency changes during photometric nights (1-2%), aperture magnitudes are a better choice than the other two types of magnitudes.

We find that even when using aperture magnitudes, the implied zeropoints oscillate on time scales of the order 1 minute, although for this particular run the rms is only ∼5 millimag (the true variations could be much larger since the data are integrated over 54 seconds). We also find that model magnitudes and psf magnitudes, when compared to aperture magnitudes, show deviations of the order ∼0.01 mag (rms). More precisely, in ∼5% of cases the disagreement exceeds 0.015 mag for the aperture vs. model magnitude comparision, and 0.02 mag for the aperture vs. psf magnitude comparision. The frequency of disagreements by more than 0.04 mag is about once in a thousand for model magnitudes, and about three times higher for psf magnitudes. In summary, the precise measurements of small (∼0.01 mag) zeropoint variations should be based on aperture magnitudes because there is a possibility that a local (temporary, usually due to fast seeing changes) problem with psf, or model, magnitudes be misinterpreted as a zeropoint variation due to changing atmospheric or cloud extinction.

The calibration summary in the u and z bands for the same short stretch of data with large extinction from run 5646 discussed above is shown in Figures 20 and 21. Although the number of calibration stars is much smaller in the u band than in the r band, the median zeropoint error is still only 0.02 mag for the median cloud extinction of 0.7 mag.

3.1.3. The Summary of Calibration Accuracy

An overall summary of calibration accuracy as a function of cloud extinction and band for one of the worst runs (in sense of final zeropoint errors, that reflect the complexity of cloud extinction structure) is shown in Figure 22, and for a run with exceptionally smooth clouds in Figure 23. As evident, the data can be calibrated with zeropoint errors smaller than 0.05 mag even for a bad case and through 1 mag thick clouds. Typically, the zeropoint errors, at a given cloud extinction, are about twice as small. In summary, *for 95% of patches, the achieved zeropoint accuracy is better than 0.05*X, where X is the cloud* *extinction.*

3.1.4. The Cloud Properties

We detect no dependence of the residuals on the stellar color or cloud thickness at a a few millimag level. This is consistent with the lack of selective absorption by clouds. Optically thick clouds are gray, which we confirm in the *gri* bands, and extend to the u and z bands. As shown in Figures 24 and 25, for most fields, the cloud extinction is similar in all bands. A few cases where there are deviations of a few tenths of a magnitude can be easily understood as due to temporal changes in the cloud opacity.

The calibration accuracy is determined by the size of calibration patch. For example, a smaller patch would suffer less from the spatial variation of cloud extinction, but it wouldn't have enough stars to beat down the noise of their individual photometric measurements ($\sim$0.02 mag). The detailed scaling of this accuracy with patch size depends on the cloud spatial structure function (SF). The geometry of the SDSS camera allows us to study the cloud SF on scales exceeding 2 degree. Figures 26 and 27 compare (independently determined) zeropoints in different columns for the same two runs discussed above. While zeropoints from different columns track each other, there can be differences exceeding a magnitude. These differences increase with the distance between the camera columns. Figure 28 shows a typical behavior: for small spatial scales (<2 degree) the SF is roughly a linear function of distance. At a 1 degree scale, the SF is typically in the range 2-10% of the cloud extinction. For example, for 3 mag thick clouds, SF at a 2 arcmin scale is <0.01 mag.

3.1.5. Implications for Surveys such as LSST

The Large Synoptic Survey Telescope is a proposed imaging survey that will attempt to maximize its observing time by accepting non-photometric conditions. At the same time, it has adopted exquisite requirements for its photometric accuracy, including 1% accuracy of its internal photometric zeropoint errors across the sky. Our analysis allows us to answer the following question: "What is the largest cloud extinction that still allows 1% accurate photometric calibration?".

A similar approach to the calibration of LSST data as presented here (assuming that a standard star catalog is available, e.g. from prior photometric nights) would benefit from several effects:

1. The calibration patches can be squares; for the same area, this results in a $\sim$5 times smaller angular scale, compared to 1:20 rectangles used to calibrate SDSS drift-scanning data. On these angular scales, the cloud structure function is roughly linear and thus the zeropoint error would be $\sim$5 times smaller, or of the order 1% or less through clouds as thick as 1 mag

2. LSST data will be deeper than SDSS by about 2-3 mag. With a conservative assumption that $\log N \propto 0.3m$ (0.6 for Euclidean counts), the surface density of stars will be about 10 times larger for LSST than for SDSS. This larger density enables 10 times smaller patches, or about 3 times smaller angular scale for calibration, resulting in another factor of 3 improvement of accuracy.

3. Fitting a smooth function for cloud opacity over several calibration patches would result in further improvements.

The first two points predict that LSST data could be calibrated with the required 1% accuracy even through 3 mag thick clouds. Given the various extrapolations, we conservatively suggest the range of 1-3 mag as the upper limit on the acceptable cloud opacity.

3.2. The Morphology of the Stellar Locus

The improved accuracy of averaged photometry provides "crispier" color-color diagrams and also reveals new morphological features. An example of such a color-color diagram is shown in Figure 29.

This is a similar plot to Figure 1 from Smolčić et al. (2004), except that *only* non-variable point sources are shown (note the absence of QSOs). The white dwarf/M dwarf "bridge" is clearly visible, as well as the locus of probable solar metallicity giants (see below) which bifurcates from the main locus at $u - g \sim 2.5$ and $g - r \sim 1$. Note also the well-defined BHB locus ($u - g \sim 1.1$ and $g - r$ from -0.3 to 0.1) and white dwarf locus at $u - g \sim 0.35$ and $g - r$ from -0.3 to $\sim$0.0). A new locus-like feature, that is *not* visible in Figure 1 from Smolčić et al., is discernible at $u - g \sim 0$ and $g - r \sim -0.2$. The great value of the accurate u band photometry is clearly evident at e.g. $g - r = -0.2$: the $u - g$ color distribution is tri-modal!

The bluest branch is consistent with He white dwarfs, and the middle branch with hydrogen white dwarfs, as supported by Bergeron white dwarf models. Kurucz models support the identification of the red bifurcating locus as probable solar metallicity giants.

The exciting fact that *one can distinguish He and H white dwarfs using photometry alone* is a consequence of the improved photometric accuracy due to averaging many epochs. Figure 30 reiterates that point. Note the striking difference between the two bottom panels: while one could be convinced that the He white dwarf sequence is a real feature in the bottom right panel, its existance is clearly evident when using the improved photometry, as shown in the bottom left panel. In summary, the multi-epoch observations enable both the identification of variable sources and much more accurate colors for non-variable sources.

4. Discussion and Conclusions

Using repeated SDSS measurements, we have constructed a catalog of about 700,000 candidate standard stars. Several independent tests suggest that both random photometric errors and internal systematic errors in photometric zeropoints are below 0.01 mag (about 2-3 times as good as individual SDSS runs) for stars brighter than (19.5, 20.5, 20.5, 20, 18.5) in *ugriz*, respectively. This is the largest catalog with multi-band optical photometry accurate to $\sim$1%, and breaks the accuracy barrier discussed by e.g. Stubbs & Tonry (2006, and references therein). These observations were not obtained for the specific purpose of calibration, but were part of regular SDSS surveying. When compared to, for example, heroic calibration efforts by Landolt, Stetson, and others, it seems justified to call the method presented here ”industrial” photometry. However, the catalog presented here is not without its own problems.

The selection of candidate stars was simply based on the absence of variability. However, it is fairly certain that not all variable sources are recognized because of the limited number of repeated observations ($\sim$10). For example, an eclipsing binary with much shorter eclipse duration than the orbital period could easily escape detection. Furthermore, some of these sources may not even be stars. A cross-correlation with the SDSS spectroscopic database shows that about 70 candidate standard stars (out of $\sim$700,000) are actually spectroscopically confirmed quasars! Apparently, a small fraction of quasars ($\sim$1%) cannot be detected by variability (at least not using the number of epochs, their time distribution, and photometric accuracy employed in this work). Indeed, we have also found three spectroscopically confirmed SDSS quasars among Stetson's standards which were observed 20-30 times and were not detected to vary. About 300 candidate standard stars have SDSS spectra classified as galaxies. However, the inspection of color-color diagrams strongly suggest that overwhelming majority are found on the stellar locus. Finaly, it is noteworthy that SDSS spectra (classified as stars) exist for about 44,000 of candidate standard stars.

Another important concern are remaining systematic errors. Effectively, we assumed that PT problems average out in many patches when deriving flatfield corrections. This may not be true at a level not much smaller than 1%. Also, the remaining gray problems due to PT are present in the catalog (though they are unlikely larger than 1%).

We illustrate several use cases for this catalog, including calibration of highly non-photometric data and robust selection of stars with peculiar colors. We discuss the upcoming large surveys and find that LSST will be able to observe in partially cloudy (non-photometric) nights because even cloudy data can be calibrated with a sufficiently dense network of calibration stars. Such a dense network will be self-calibrated by LSST very soon after the first light. Given such a network, SDSS experience suggests that LSST can maintain its required photometric calibration accuracy of 1% even when observing through 1-3 mag thick clouds.

Perhaps the most exciting conclusion of this work is that it may become obsolete in only a few years due to the advent of next-generation surveys such as Pan-STARSS and LSST.

Acknowledgments

We are thankful to Peter Stetson for his most useful comments and for providing to us his latest standard star photometry.

Funding for the creation and distribution of the SDSS Archive has been provided by the Alfred P. Sloan Foundation, the Participating Institutions, the National Aeronautics and Space Administration, the National Science Foundation, the U.S. Department of Energy, the Japanese Monbukagakusho, and the Max Planck Society. The SDSS Web site is http://www.sdss.org/.

The SDSS is managed by the Astrophysical Research Consortium (ARC) for the Participating Institutions. The Participating Institutions are The University of Chicago, Fermilab, the Institute for Advanced Study, the Japan Participation Group, The Johns Hopkins University, the Korean Scientist Group, Los Alamos National Laboratory, the Max-Planck-Institute for Astronomy (MPIA), the Max-Planck-Institute for Astrophysics (MPA), New Mexico State University, University of Pittsburgh, University of Portsmouth, Princeton University, the United States Naval Observatory, and the University of Washington.

REFERENCES

Abazajian, K., Adelman, J.K., Agueros, M., et al. 2003, AJ, 126, 2081

Baldry, I.K, Glazebrook, K., Brinkmann, J., et al. 2004, ApJ, 600, 681

Gunn, J.E., Carr, M., Rockosi, C., et al. 1998, AJ, 116, 3040

Hogg, D.W., Finkbeiner, D.P., Schlegel, D.J. & Gunn, J.E. 2002, AJ, 122, 2129

Ivezić, Ž., Goldston, J., Finlator, K., et al. 2000, AJ, 120, 963

Ivezić, Ž., Lupton, R.H., Anderson, S., et al. 2003a, Proceedings of the Workshop *Variability with Wide Field Imagers*, Mem. Soc. Ast. It., 74, 978 (also astro-ph/0301400)

Ivezić, Ž., Lupton, R.H., Schlegel, D., et al. 2004a, AN, 325, 583

Ivezić, Ž., Lupton, R.H., Johnston, D., et al. 2004b, in *AGN Physics with the Sloan Digital Sky Survey*, eds. G.T. Richards and P.B. Hall, ASP Conference Series, Vol. 311, p. 437 (also astro-ph/0310566)

Ivezić, Ž., Vivas, A.K., Lupton, R.H. & Zinn, R. 2005, AJ, 129, 1096

Jurić, M., Ivezić, Ž., Lupton, R. H., et al. 2002, AJ, 124, 1776

Kaiser, N., Aussel, It., Burke, B.e., et al. 2002, in "Survey and Other Telescope Technologies and Discoveries", Tyson, J.A. & Wolff, S., eds. Proceedings of the SPIE, 4836, 154

Landolt, A.U. 1992, AJ, 104, 340

Lupton, R.H. 1993, *Statistics in Theory and Practice*, Princeton University Press, Princeton, New Jersey

Lupton, R.H., Gunn, J.E., & Szalay, A. 1999, AJ, 118, 1406

Lupton, R.H., Ivezić, Ž., Gunn, J.E., Knapp, G.R., Strauss, M.A. & Yasuda, N. 2003, in "Survey and Other Telescope Technologies and Discoveries", Tyson, J.A. & Wolff, S., eds. Proceedings of the SPIE, 4836, 350

Oke, J.B., & Gunn, J.E. 1983, ApJ, 266, 713

Pier, J.R., Munn, J.A., Hindsley, R.B., Hennesy, G.S., Kent, S.M., Lupton, R.H. & Ivezić, Ž. 2003, AJ, 125, 1559

Schlegel, D., Finkbeiner,D.P. & Davis, M. 1998, ApJ500, 525

Sesar, B., Svilković, D., Ivezić, Ž., et al. 2006, AJ, 131, 2801

Smith, J.A., Tucker, D.L., Kent, S.M., et al. 2002, AJ, 123, 2121

Smolčić, V., Ivezić, Ž., Knapp, G.R., et al. 2004, ApJ, 615, L141

Stetson, P.B. 2000, PASP, 112, 925

Stetson, P.B. 2005, PASP, 117, 563

Stoughton, C., Lupton, R.H., Bernardi, M., et al. 2002, AJ, 123, 485

Strateva, I., Ivezić, Ž., Knapp, G.R., et al. 2001, AJ, 122, 1861

Strateva, I., Ivezić, Ž., Knapp, G.R., et al. 2001, AJ, 122, 1861

Stubbs, C.W. & Tonry, J.L. 2006, astro-ph/0604285

Tucker, D., et al. 2005, AJ, submitted (MT Pipeline)

Tyson, J.A. 2002, in *Survey and Other Telescope Technologies and Discoveries*, Tyson, J.A. & Wolff, S., eds. Proceedings of the SPIE, 4836, 10

York, D.G., Adelman, J., Anderson, S., et al. 2000, AJ, 120, 1579

Table 1. The Effect of Repeated Measurements on the Width of the Stellar Locus

PC	width 1 obs[a]	width N obs[b]	median[c]	width for PC/PCerror[d]
s	0.031	0.019	0.003	3.02
w	0.025	0.010	0.001	1.82
x	0.042	0.034	0.001	5.34
y	0.023	0.009	0.000	1.64

[a]The locus width determined using single-epoch SDSS observations (in mag).

[b]The locus width determined using multiple SDSS observations (in mag).

[c]The median principal color determined using multiple SDSS observations (in mag).

[d]The locus width normalized by expected measurement errors.

Table 2. The Flatfield Corrections[a]

band	width[b]	min[c]	max[d]
u	0.019	-0.045	0.041
g	0.008	-0.018	0.025
r	0.006	-0.015	0.017
i	0.006	-0.013	0.018
z	0.012	-0.031	0.025

[a]The r band correction is determined using observations by the Photometric Telescope, and the *ugiz* corrections are determined using the stellar locus method.

[b]The root-mean-square scatter for applied flatfield corrections (in mag).

[c]The minimum value of the applied correction (in mag).

[d]The maximum value of the applied correction (in mag).

Table 3. The statistics of median PT-2.5m residuals

band	<>[a]	width[b]	min[c]	max[d]	N[e]	<>[f]
u	-0.002	0.009	-0.018	0.023	175	0.005
g	0.006	0.007	-0.004	0.017	647	0.005
r	0.003	0.007	-0.007	0.010	627	0.003
i	0.004	0.007	-0.010	0.017	621	0.002
z	0.001	0.008	-0.016	0.015	286	-0.002

[a]The median value for the bin medians (in mag). There are 24 bins, distributed inhomogeneously in the RA direction.

[b]The root-mean-square scatter for the bin medians (in mag).

[c]The minimum value for the median residuals (in mag).

[d]The maximum value for the median residuals (in mag).

[e]The median number of stars per bin.

[f]The median value of the residuals for stars with colors within 0.02 mag from the crossing colors (in mag).

Table 4. Residuals from the mean color-redshift relation for red galaxies.

color	rms(Dec)^b	χ(Dec)	rms(RA)^c	χ(RA)
$u-g$	21	1.5	18	1.3
$g-r$	4	1.3	12	2.6
$r-i$	3	1.3	6	3.5
$i-z$	6	2.6	6	2.9

[a]The table lists the widths of color-residual distributions (in millimag), and the widths of distributions of residuals normalized by statistical noise (χ), using mean color-redshift relations (see text).

[b]The rms for Dec direction, using 0.025 deg wide bins (0.1 deg for the $u-g$ color).

[c]The rms for RA direction, using 2 deg wide bins (5 deg for the $u-g$ color).

Table 5. Comparison with Stetson's standards: I. SDSS to BVRI transformations

color	$<>^{a}_{med}$	σ^{b}_{med}	χ^{c}_{med}	$<>^{d}_{all}$	σ^{e}_{all}	A	B	C	D[f]
$B-g$	0.5	3.4	0.6	−0.7	35	0.019	−0.1673	0.5280	0.0887
$V-g$	0.1	2.7	0.6	3.0	20	0.060	−0.2247	−0.1286	−0.1074
$R-r$	2.9	6.0	1.4	1.1	16	−0.005	0.0125	−0.0946	−0.1467
$I-i$	1.3	4.6	1.0	0.5	19	−0.004	0.0082	−0.0798	−0.3709

[a]The median value of residuals (differences between the measured values of colors listed in the first column and those synthesized using Eq. 9) in 0.2 mag wide $g-i$ bins for stars with $0.3 < g-i < 2.3$ (in millimag). The residuals measure the level of systematics in the *ugriz*-to-*BVRI* photometric transformations introduced by adopted analytic form (see text).

[b]The root-mean-square scatter for residuals evaluated in 0.2 mag wide $g-i$ bins (in millimag).

[c]The root-mean-square scatter for residuals normalized by statistical noise (in millimag). The listed values are $\sim$1, which indicates that the scatter around adopted photometric transformations listed under b) is consistent with expected noise.

[d]The median value of (unbinned) residuals evaluated for all stars with $0.3 < g-i < 2.3$ (in millimag).

[e]The root-mean-square scatter for residuals evaluated for all stars with $0.3 < g-i < 2.3$ (in millimag).

[e]Coefficients A–D needed to transform SDSS photometry to the Landolt BVRI system (see Eq. 9).

Table 6. Comparison with Stetson's standards: II. Photometric zeropoint variations

color	$<>^a_{R1}$	σ^b_{R1}	N^c_{R1}	$<>^a_{R2}$	σ^b_{R2}	N^c_{R2}	$<>^a_{R3}$	σ^b_{R3}	N^c_{R3}	$<>^a_{R4}$	σ^b_{R4}	N^c_{R4}
$B-g$	−29	0.021	92	6	0.027	165	8	0.042	155	−4	0.027	281
$V-g$	0	0.017	99	0	0.015	217	6	0.025	161	17	0.019	282
$R-r$	−6	0.016	58	4	0.016	135	−8	0.012	11	39	0.027	60
$I-i$	−11	0.016	94	6	0.018	205	2	0.016	124	19	0.015	47

[a]The median value of (unbinned) residuals evaluated for all stars with 0.3< $g-i$ <2.3 (in mag) from regions 1-4, defined as: **R1:** RA∼325, Dec<0; **R2:** RA∼15; **R3:** RA∼55; **R4:** RA∼325, Dec>0.

[b]The root-mean-square scatter for residuals evaluated for all stars with 0.3< $g-i$ <2.3 (in mag) from regions 1-4, defined above.

[c]The number of stars in each region.

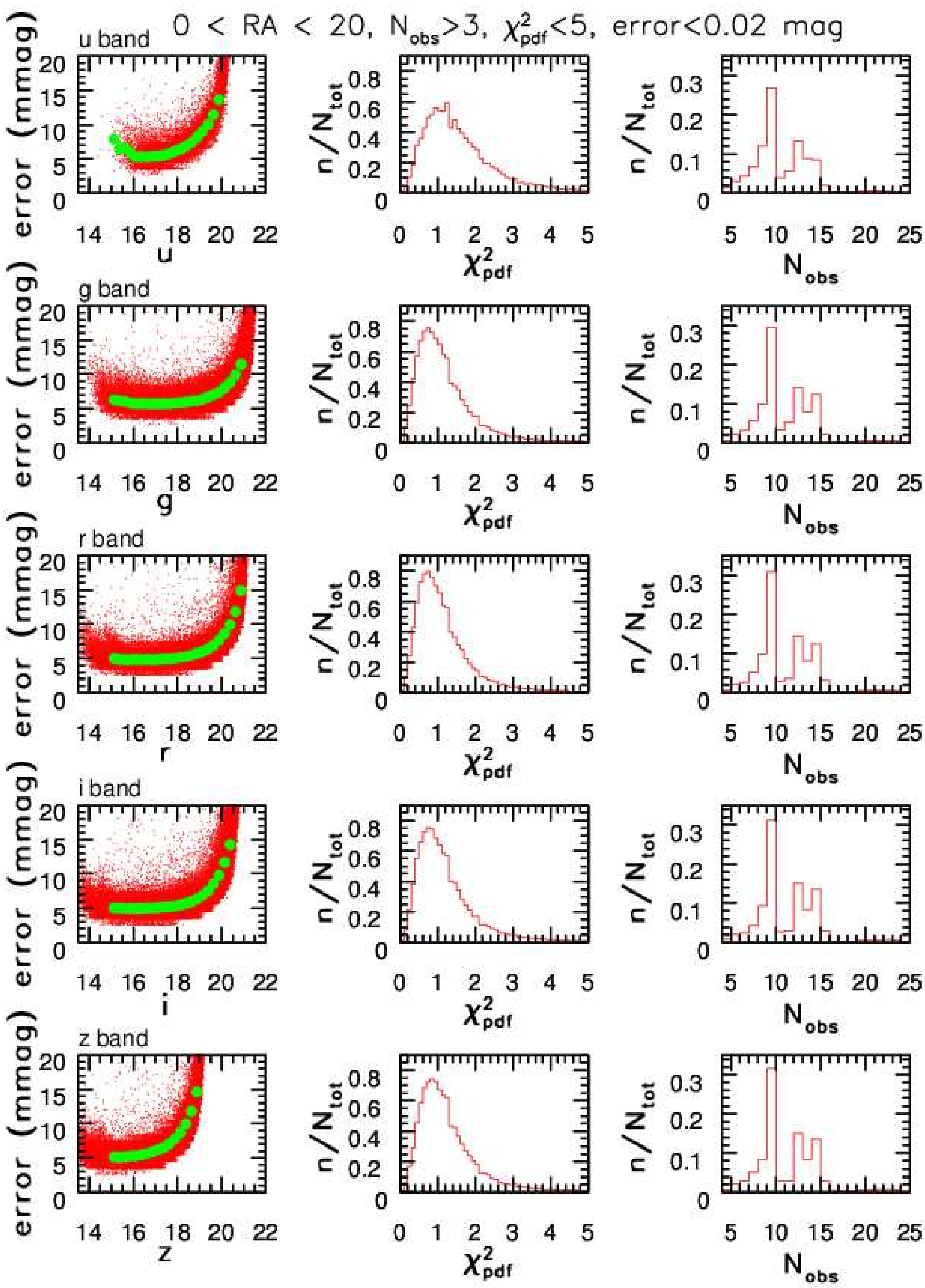

Fig. 1.— The distributions of median magnitude, its error, χ^2_{pdf} and the number of observations for a subset of multiply observed stars from SDSS stripe 82. Each row corresponds to one SDSS band. The small red dots in the first column are individual stars, and the large green dots are the median errors. The errors are reliable, as the χ^2 per degree of freedom distributions in the middle column demonstrate. The distributions of the number of observations are shown in the last column.

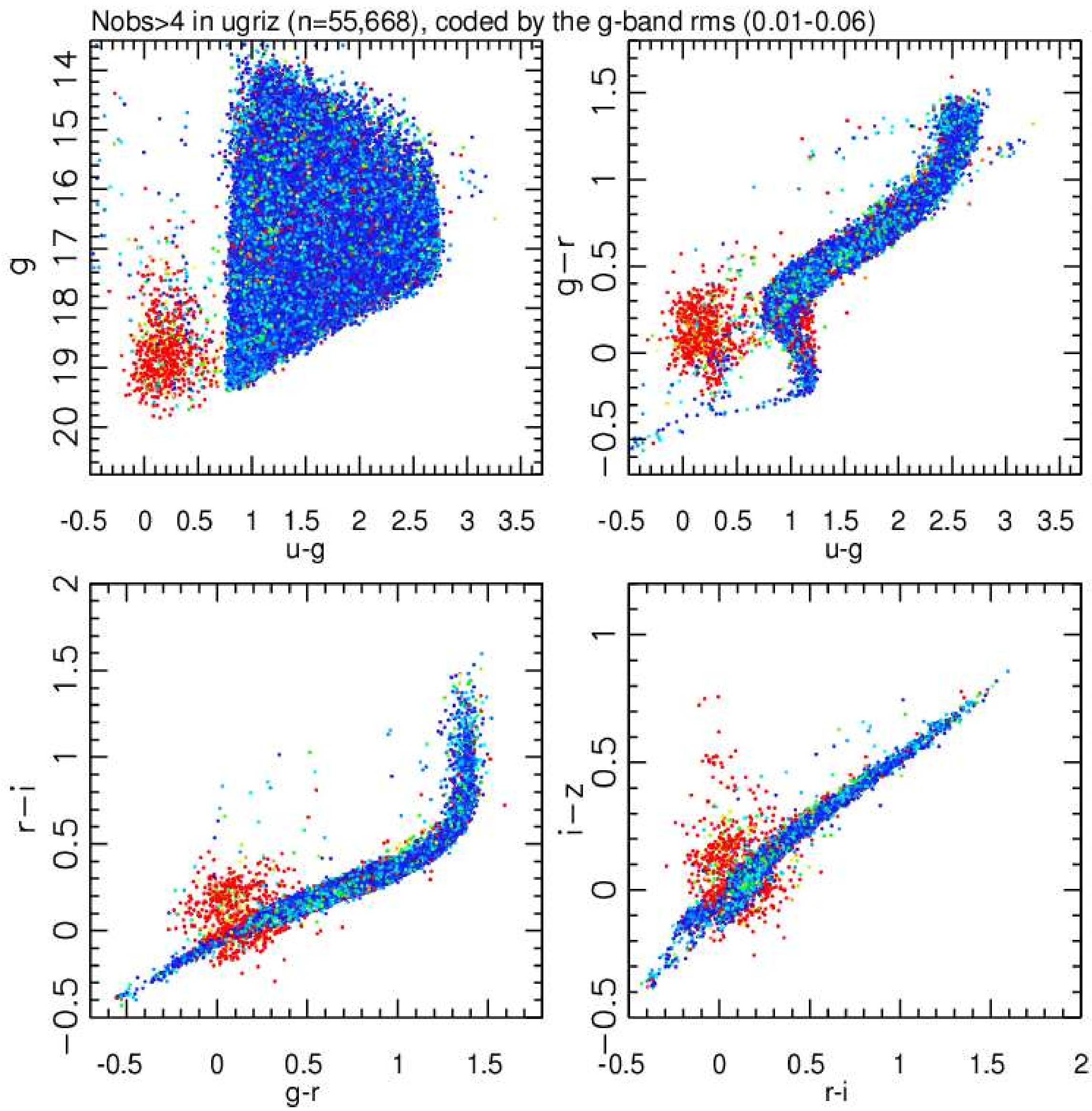

Fig. 2.— The color-magnitude and color-color distributions of multiply observed stars from SDSS stripe 82, that have at least four observations in each band. The points are color-coded according to the observed rms scatter in the g band (0.01–0.06, from blue to red). Note how QSOs ($u - g < 0.6$) and RR Lyrae ($u - g \sim 1.1$) stand out as variable sources (red points). The diagonal faint cutoff in the top left panel is a result of the faint limit in the u band ($u < 20.5$).

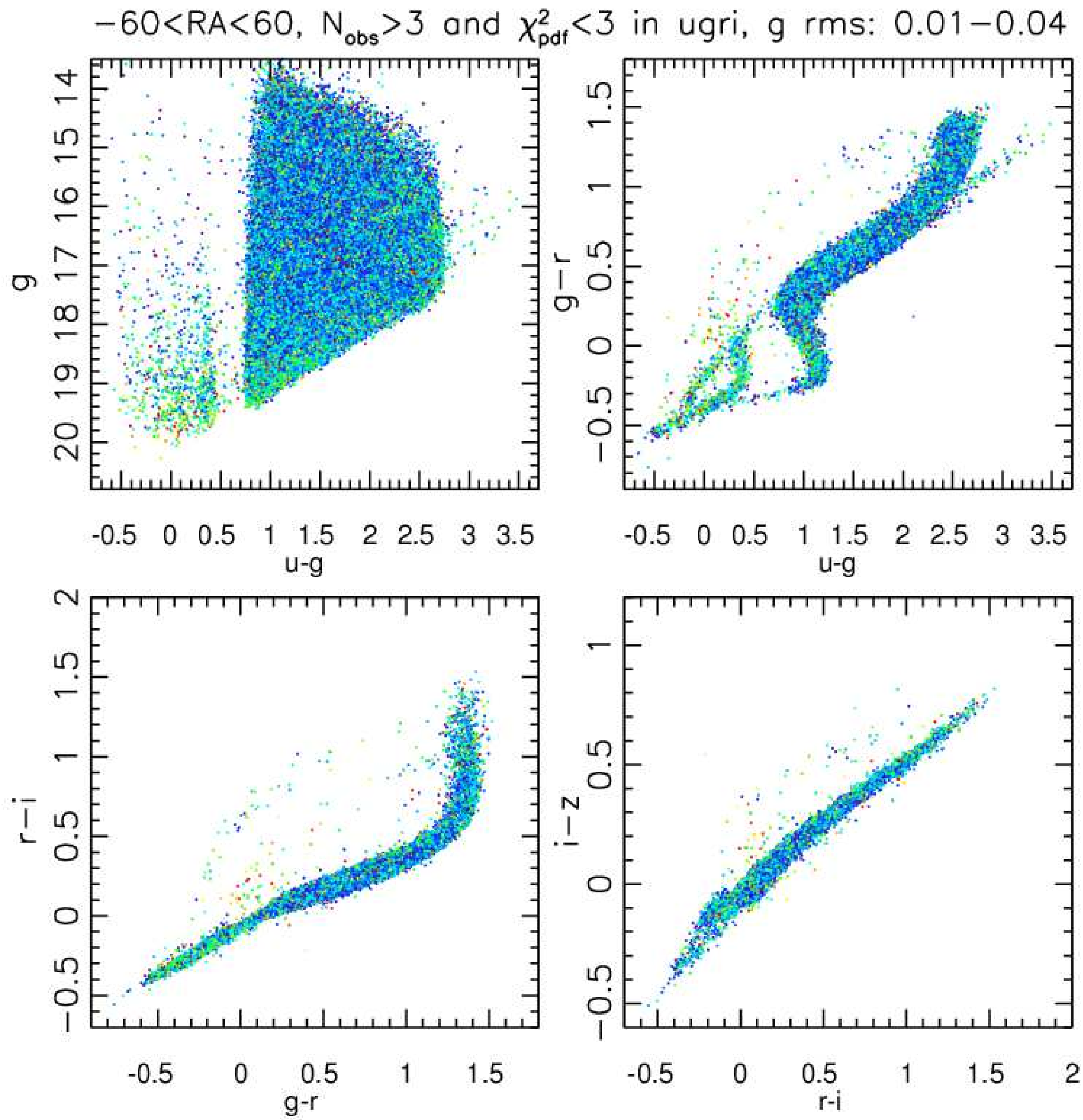

Fig. 3.— Analogous to Figure 2, except that only non-variable sources are shown, and the range for color-coding by the observed rms scatter in the g band is 0.01–0.04 (from blue to red).

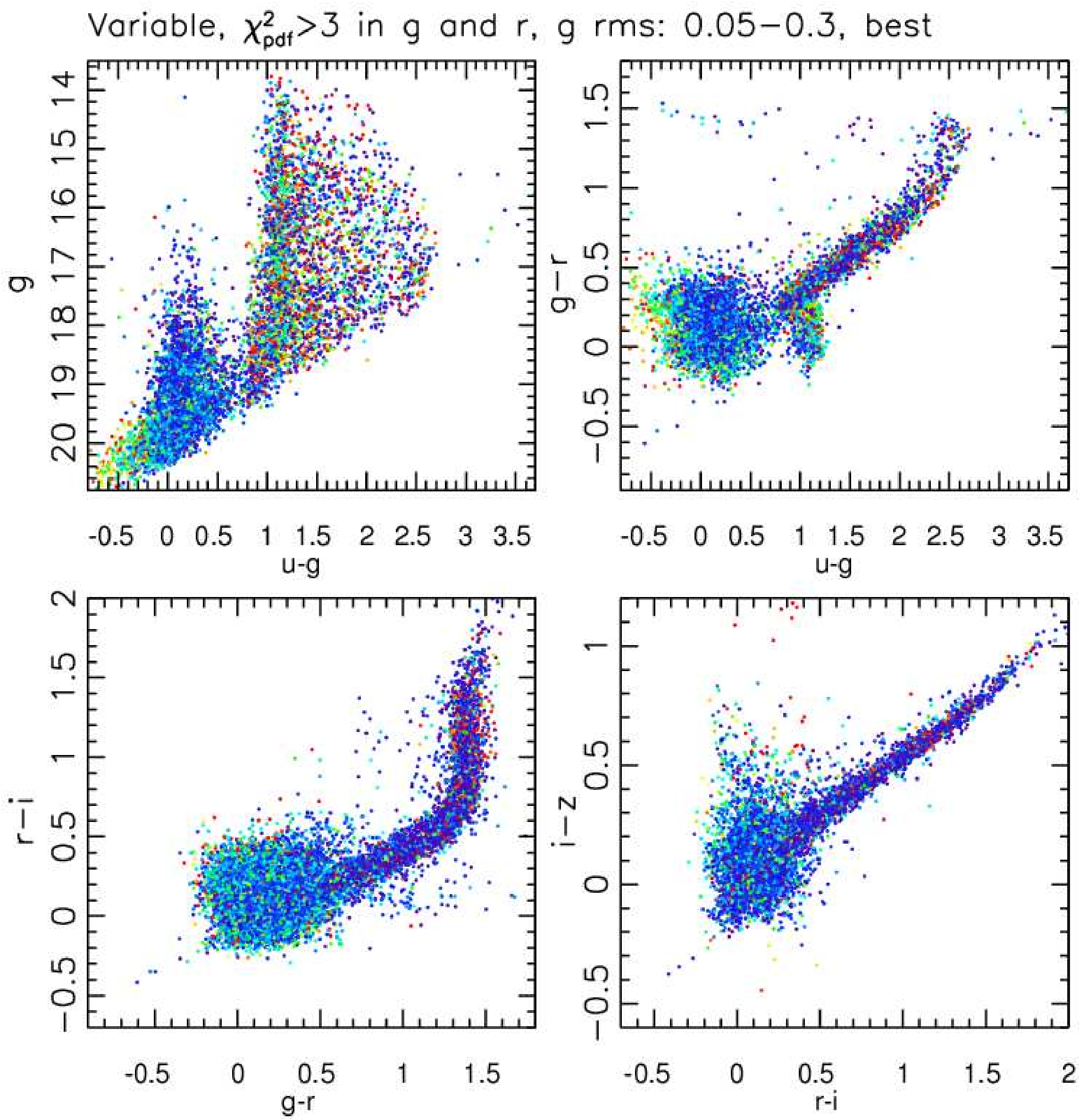

Fig. 4.— Analogous to Figure 2, except that only variable sources are shown, and with a different color coding (0.05–0.30 range of the g band rms, instead of 0.01–0.06).

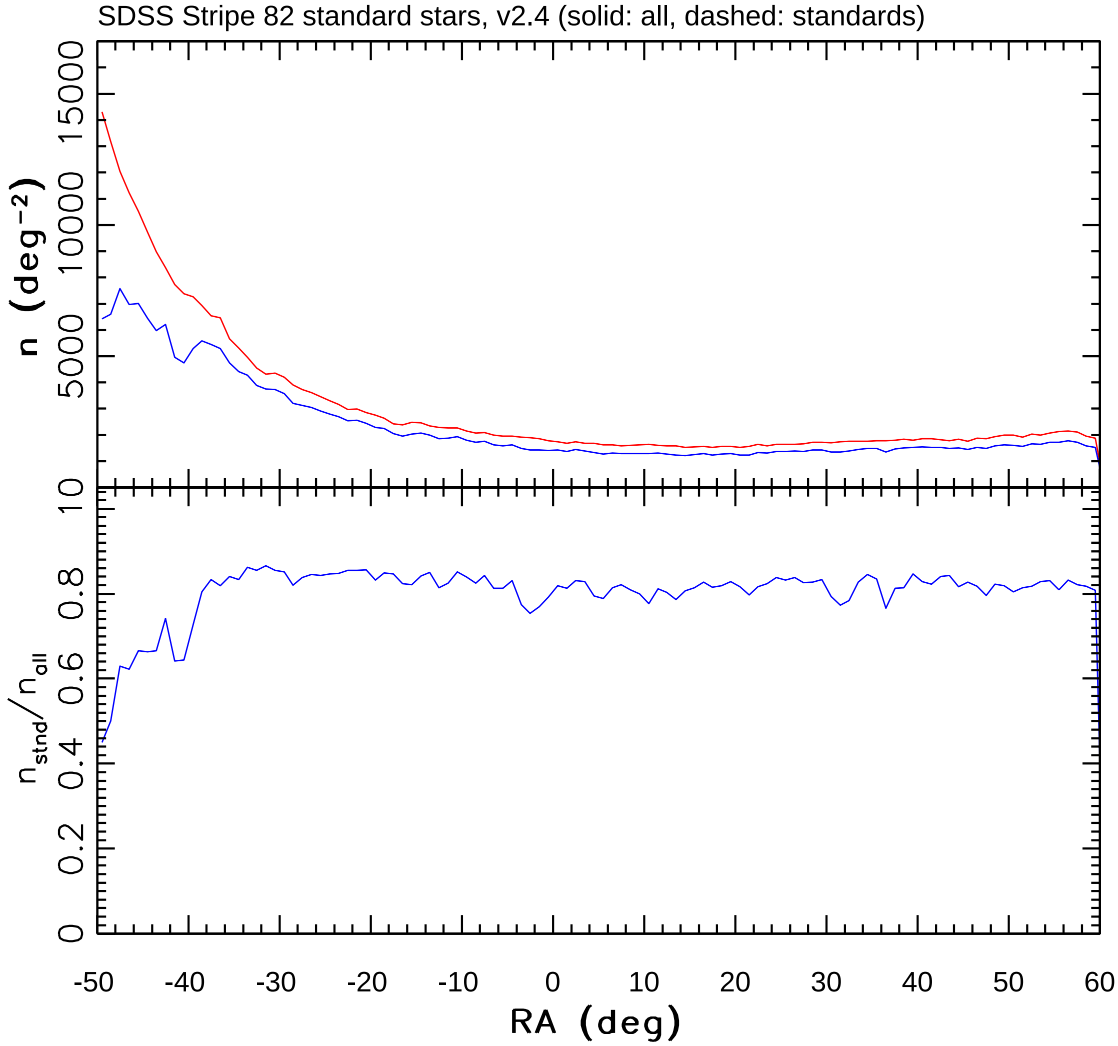

Fig. 5.— The top panel shows the sky density of all the point sources with at least 4 observations in each of the g, r and i bands (solid), and of selected candidate standard (non-variable) stars (dashed). The bottom panel shows the ratio of the two curves shown in the top panel. For reference, galactic coordinates, (l,b), are (46,−24), (96,−60) and (190,−37) for RA=−50, 0 and 60 (at Dec=0).

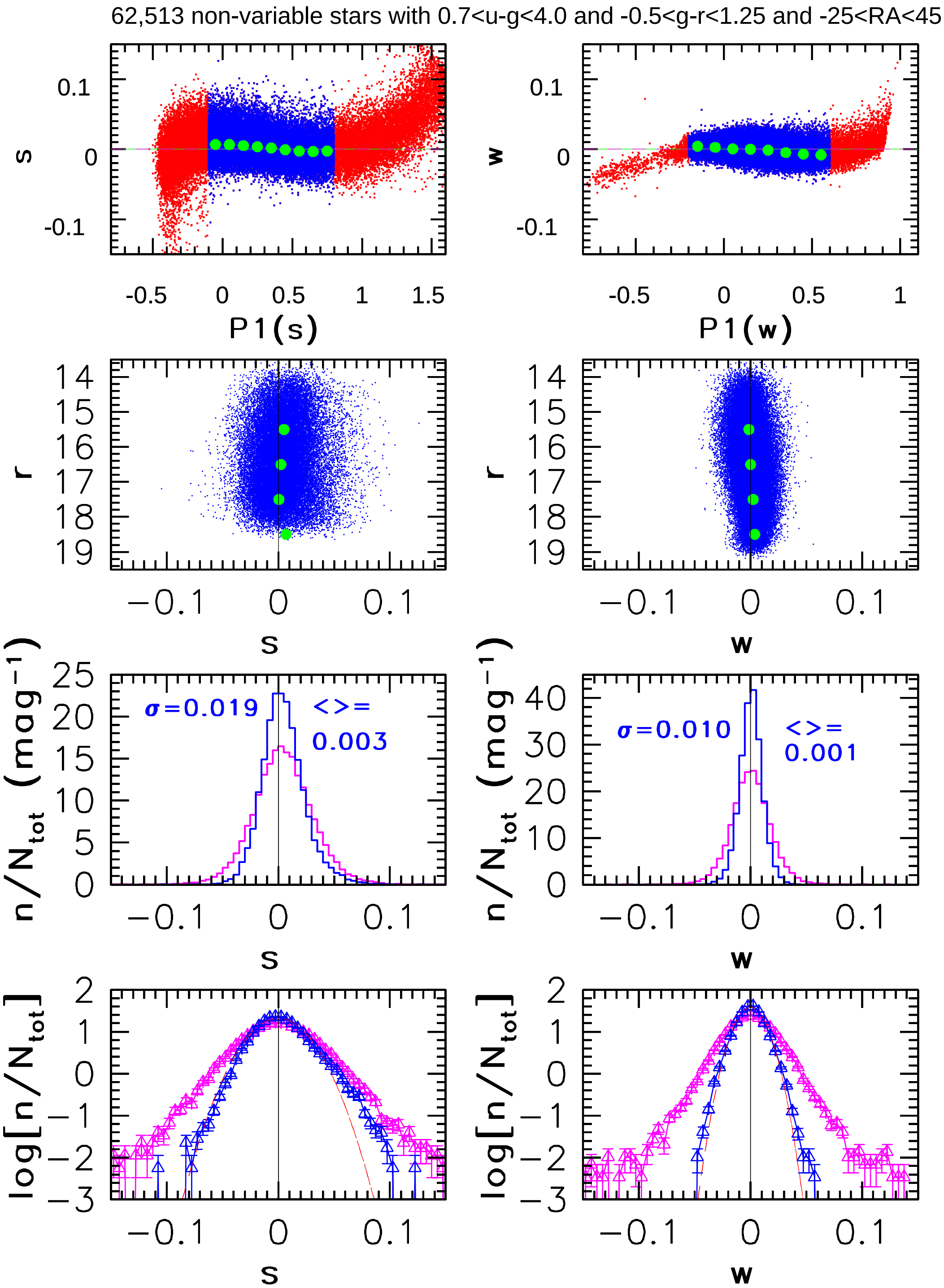

Fig. 6.— The top two panels show two projections of the stellar locus (in the *ugr* and *gri* planes), and the next two panels show their dependence on magnitude for stars shown by blue symbols in the top row. The large green dots show median values in bins of colors and magnitude. The last two rows show histograms for each principal color on linear and logarithmic scale (essentially the locus cross-sections). The blue (narrow) histograms are constructed using the averaged photometry, and the magenta histograms are based on single-epoch photometry. The best-fit Gaussians, with parameters listed in the third row, are shown by the dashed lines in the fourth row (only for the averaged photometry).

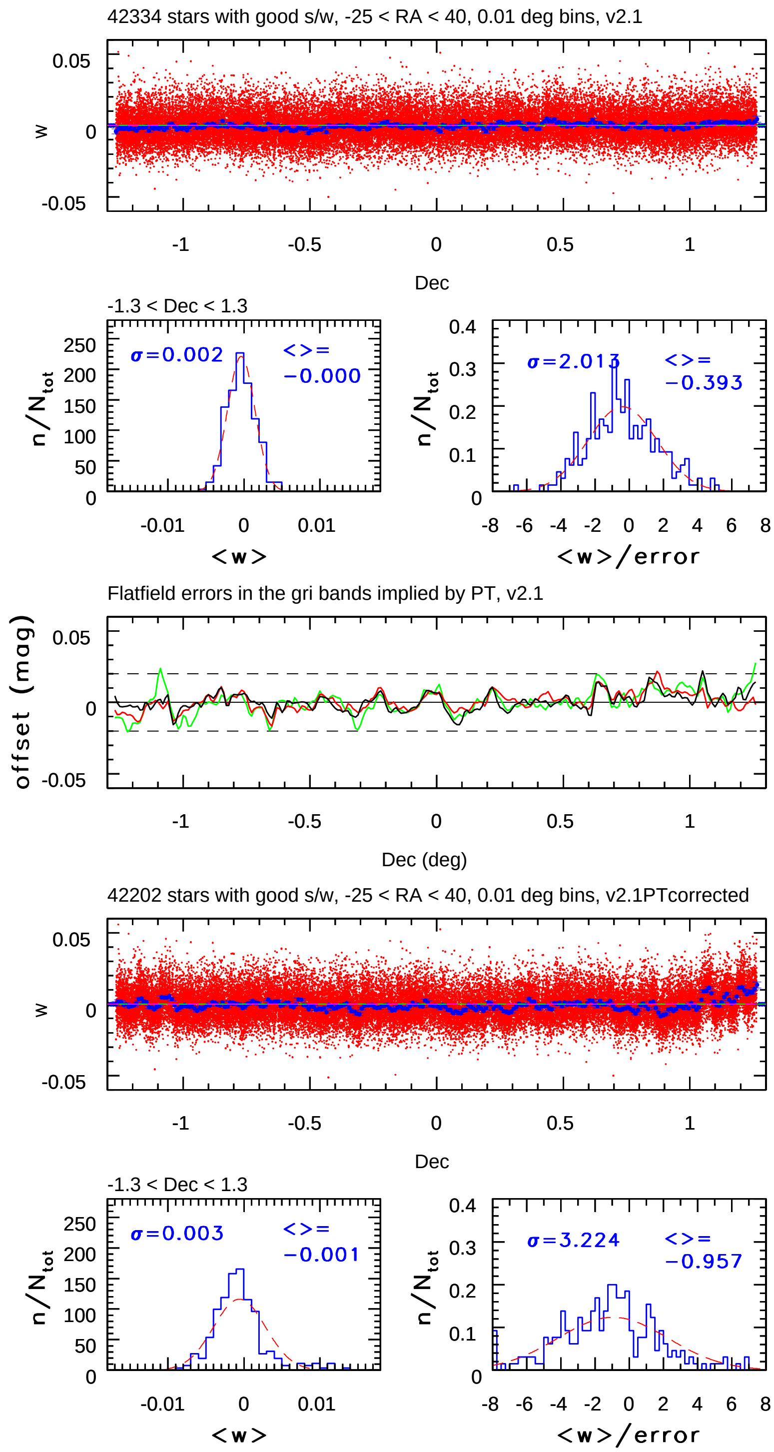

Fig. 7.— The top panel shows the dependence of the median w principal color (large blue symbols) on Dec, for a sample of color-selected stars (dots) from the blue part of the stellar locus in the $r-i$ vs. $g-r$ color-color diagram. The two panels in the second row shows the distribution of these medians (left) and the distribution of the same medians normalized by the statistical noise (right). The middle panel shows the distribution of the residuals between the PT photometry and averaged magnitudes in the gri bands. The bottom two rows are analogous to the top two rows, except that averaged magnitudes where corrected by the residuals shown in the middle panel. Note the increased scatter in the distribution of median w color.

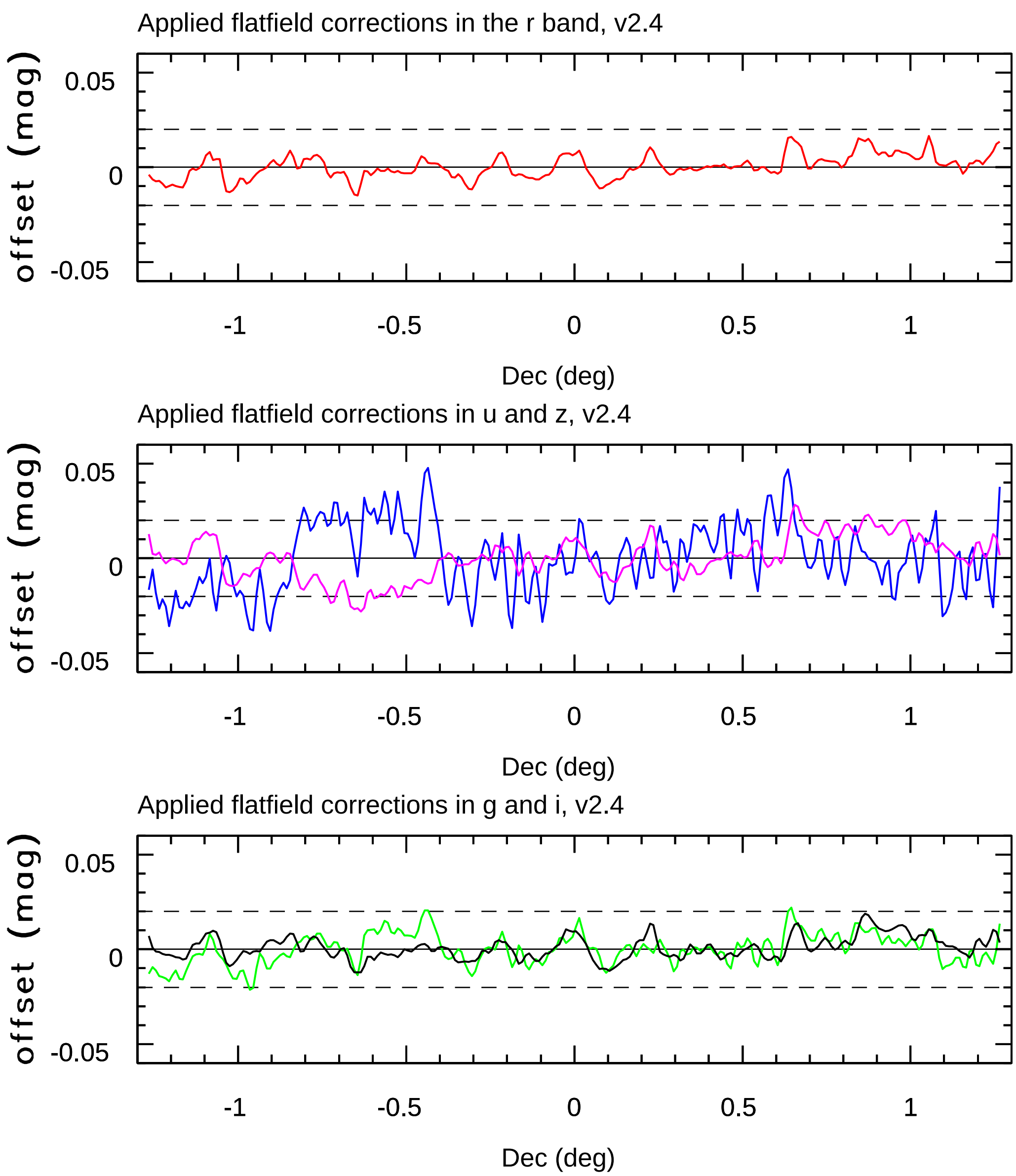

Fig. 8.— The top panel shows the applied flatfield correction in the r band, that was derived as the mean of the PT-2.5m photometric residuals shown in the middle panel in Figure 7. The middle and bottom panels show the applied flatfield corrections in other four bands (middle: uz, bottom: gi), that were derived using the stellar locus colors. The low-order statistics for these corrections are listed in Table 2.

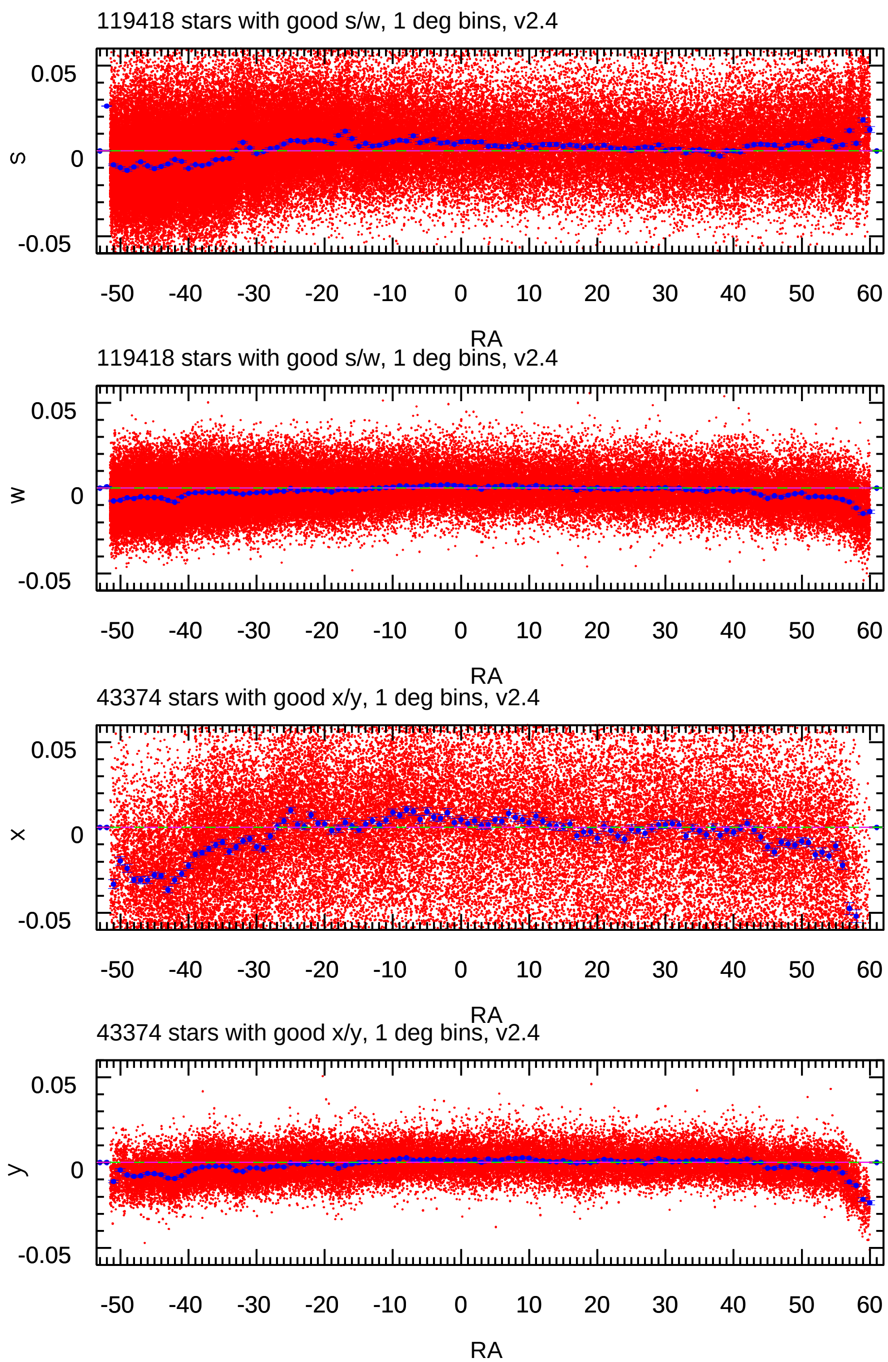

Fig. 9.— The panels show the dependence of the position of the stellar locus in *ugriz* color space, as parametrized by the median principal colors *swxy*, as a function of RA. Close to the edges, the median colors deviate significantly from 0. This is due to the failure of the stellar locus method, rather than due to calibration problems (see the next figure).

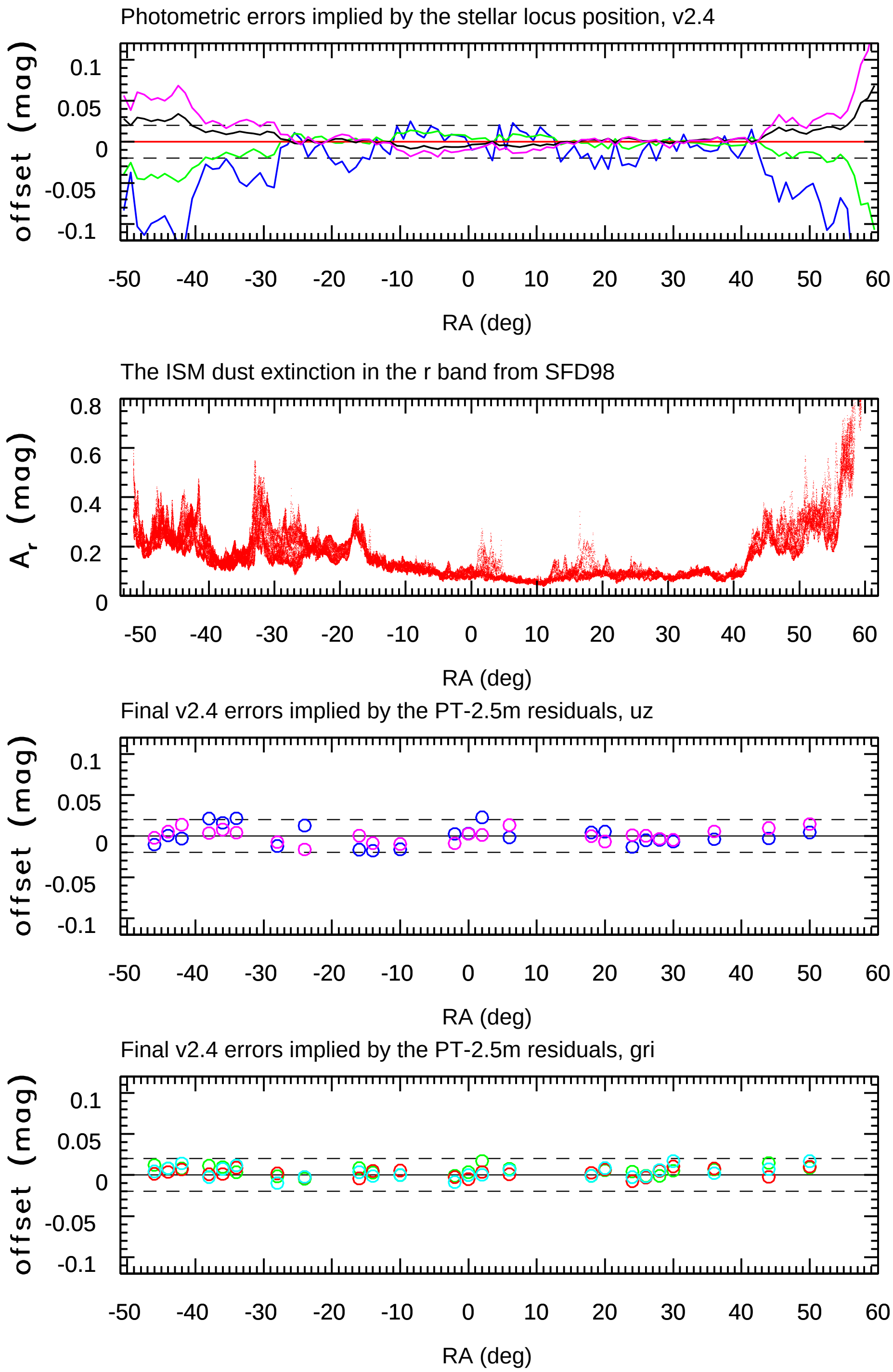

Fig. 10.— The top panel shows the implied photometric zeropoint errors based on the stellar locus method (*ugriz* from the bottom to the top at either edge). While the implied errors are small for $-25 < \mathrm{RA} < 40$, they become exceedingly large outside this range. This is due to problems with the stellar locus method rather than due to problems with calibration. The second panel shows the r band extinction derived from the Schlegel, Finkbeiner & Davis (1998) maps. The bottom two panels show the median residuals between the PT photometry and averaged magnitudes in the uz (third row) and gri bands (bottom row). The low-order statistics for these residuals are listed in Table 3.

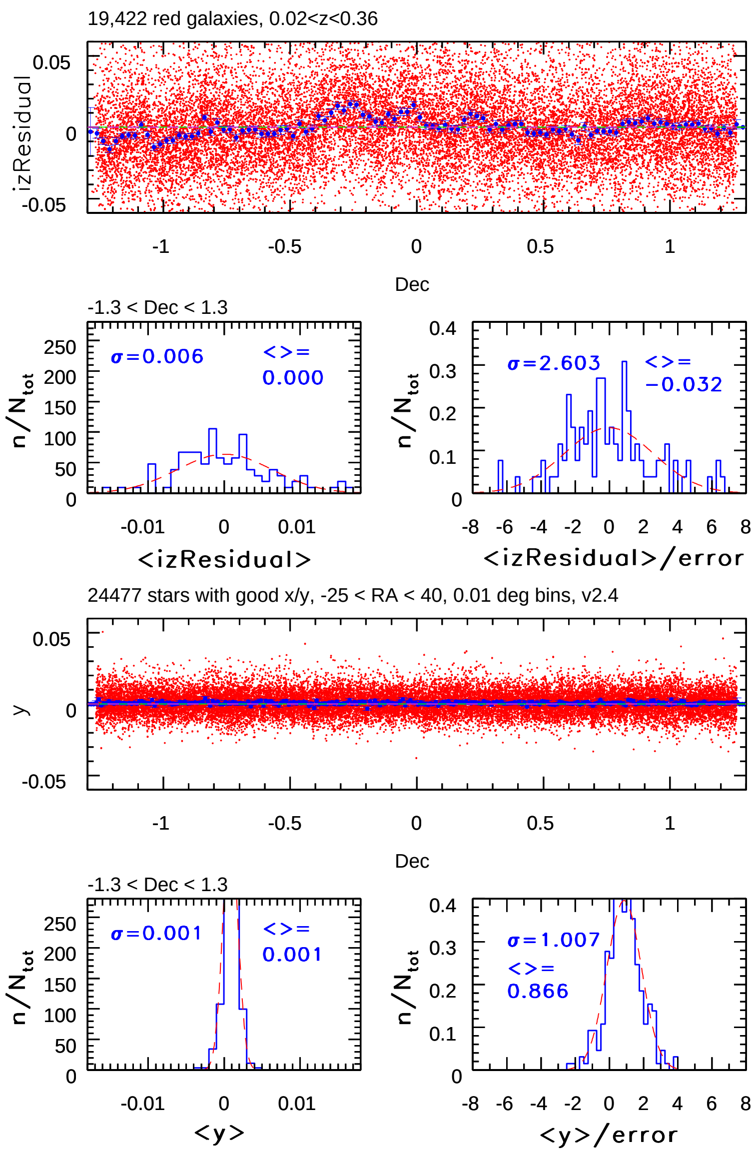

Fig. 11.— The top panel shows the dependence of the $i - z$ color residuals (with respect to a color-redshift relation) for red galaxies as a function of Dec. The dots are individual galaxies, and the large symbols with error bars are medians evaluated in 0.025 deg wide bins. The two panels in the second row shows the distribution of these medians (left) and the distribution of the same medians normalized by the statistical noise (right). The panel in the third row and two bottom panels are analogous, except that they show the position of stellar locus in the $i - z$ vs. $r - i$ diagram, using the y principal color (the implied scatter in the $i - z$ color is about twice as large as the scatter of the y color). The stellar colors rule out a possibility that the variation seen in the top panel is due to photometric zeropoint errors.

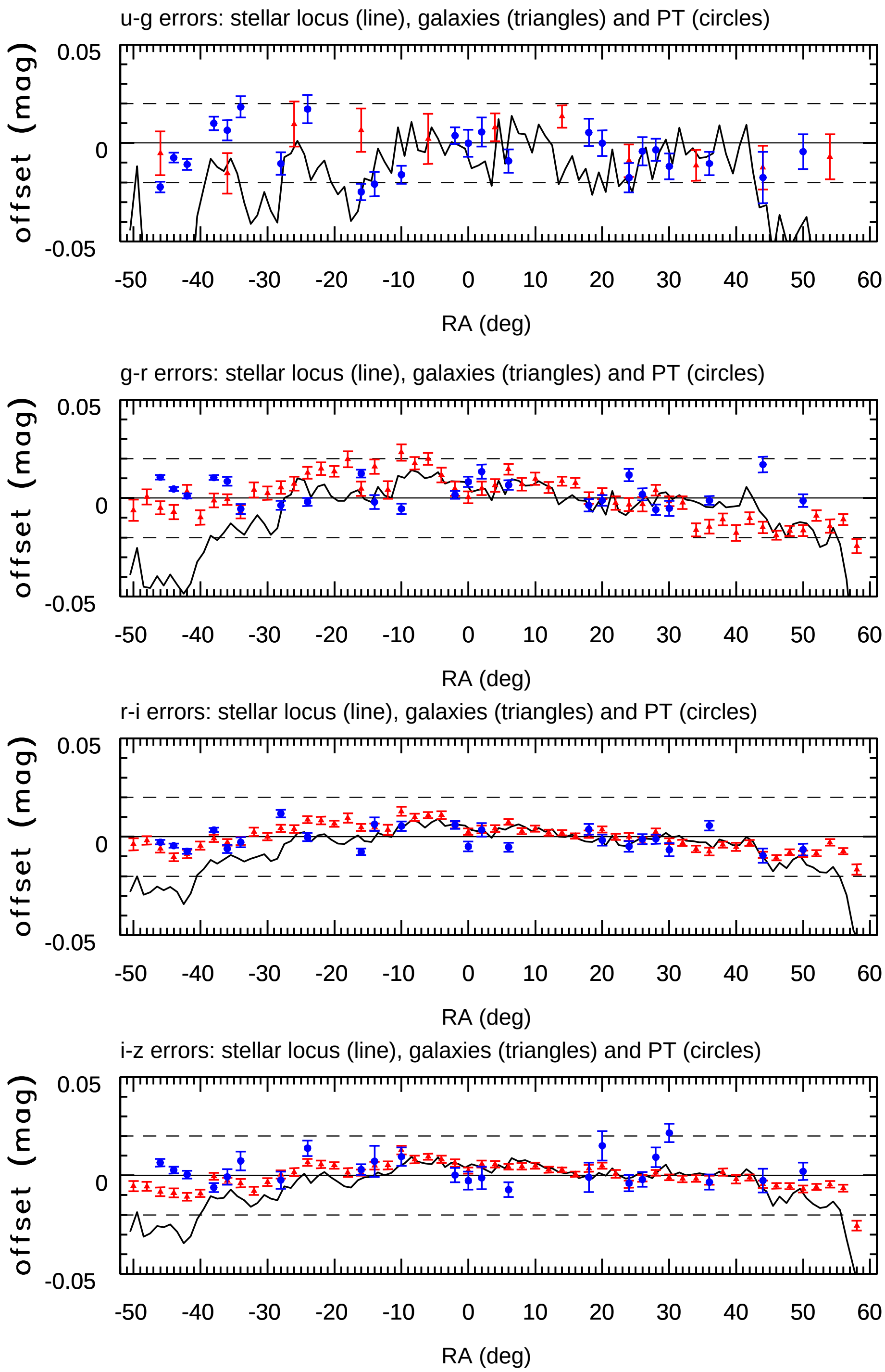

Fig. 12.— The comparison of systematic color errors implied by different methods. Note that the errors implied by the stellar locus method (line) become exceedingly large outside the $-25 < \mathrm{RA} < 40$ range. As galaxy colors (triangles) and a direct comparison with SDSS secondary standard star network (circles) suggest, this is due to problems with the stellar locus method rather than due to problems with calibration.

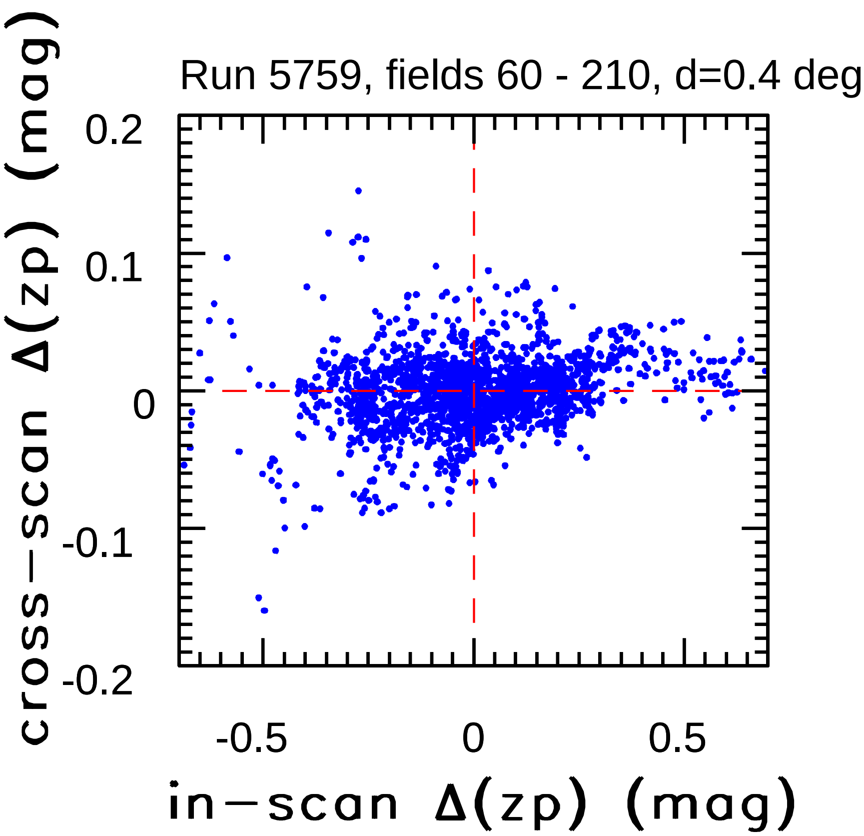

Fig. 13.— The comparison of cloud extinction gradients in the in-scan (RA, horizontal axis) and cross-scan (Dec, vertical axis) directions for SDSS run 5759, on a spatial scale of 0.4 deg. Note different axis scales. For this particular run, the distribution width is 9.6 times larger for the in-scan than for the cross-scan direction. This is a consequence of the cloud motion relative to the boresight, and the drift-scanning technique.

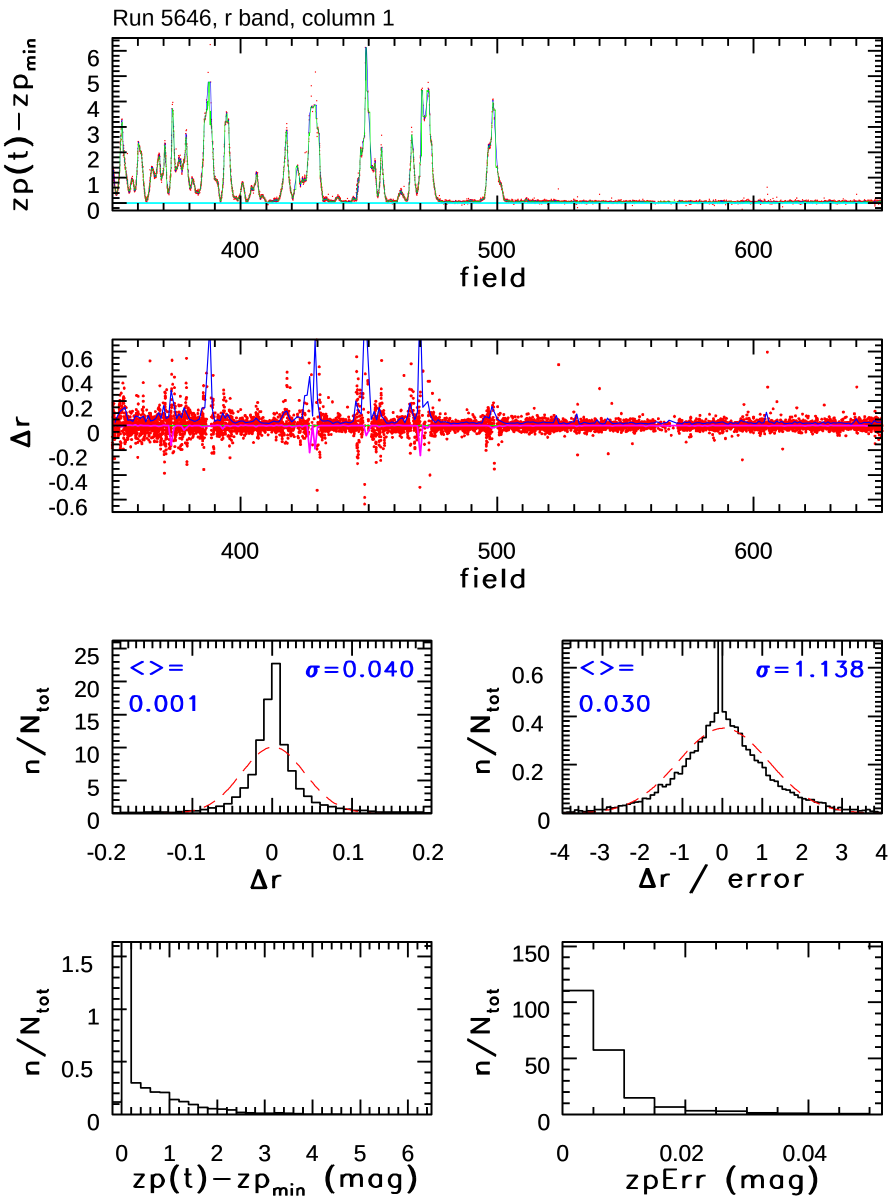

Fig. 14.— The top panel summarizes the behavior of cloud extinction in the r band over three hours during SDSS-II run 5646 (one field corresponds to 36 seconds of time). The adopted zeropoint is shown by the green line. Individual calibration stars are shown by dots, and the blue line (barely visible under the green line) shows median-smoothed values that are input for calibration. The calibration residuals for each star are shown by dots in the second panel. The blue line in this panel shows the root-mean-square scatter for these residuals evaluated for each field. The distribution of these residuals is shown in the left panel in the third row as the solid line. The median and equivalent Gaussian σ evaluated from the inter-quartile range are also shown in the panel, as well as a Gaussian corresponding to these parameters (dashed line). The right panel is analogous, except that the residuals are normalized by the expected errors. The distribution of implied cloud extinction is shown in the bottom left panel, and the distribution of errors for adopted photometric zeropoints in the bottom right panel.

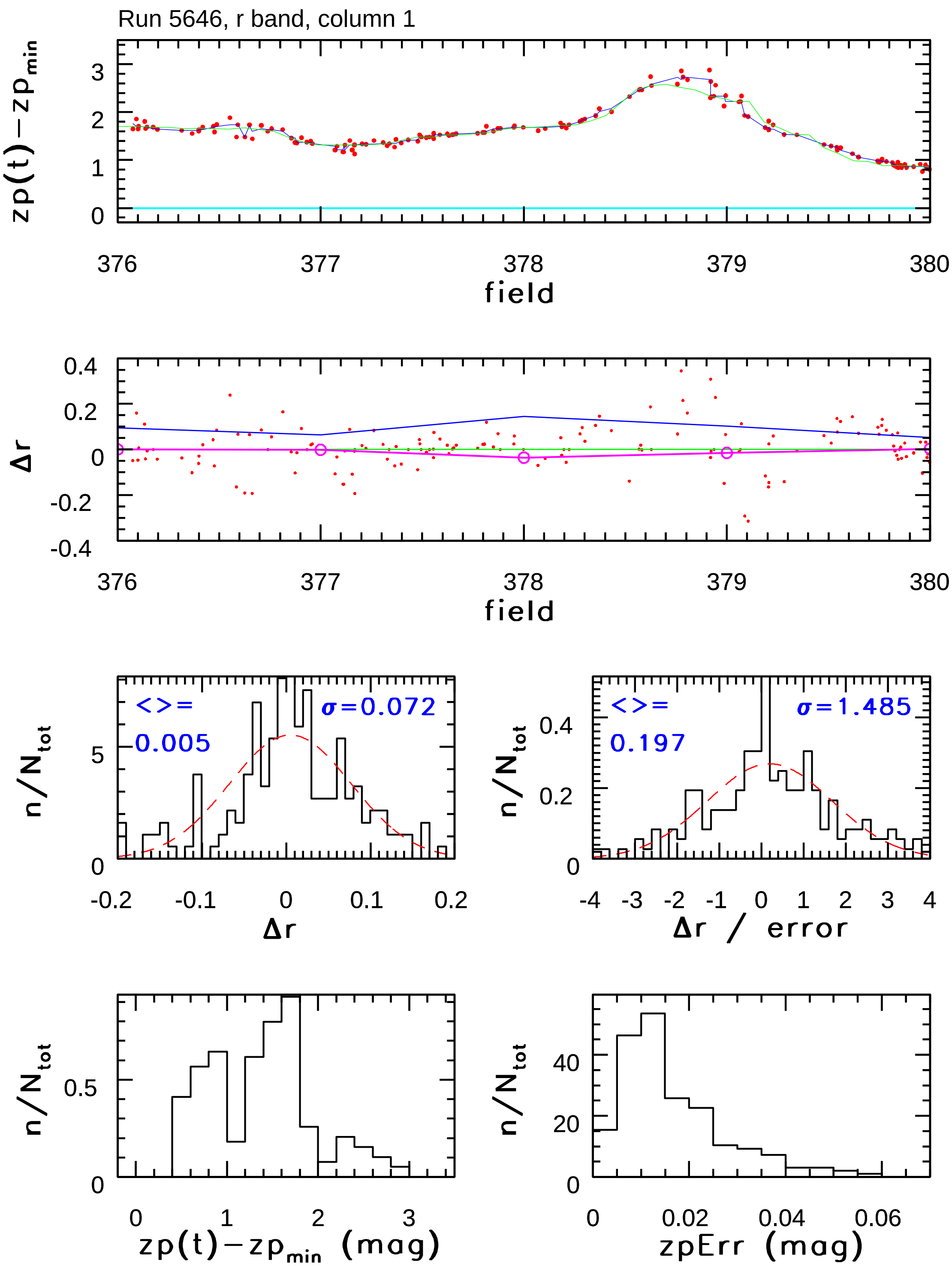

Fig. 15.— Analogous to Fig. 14, except that only 2 minutes worth of data with large cloud extinction is shown. Note that the changes in cloud extinction are resolved down to time scales well below 10 seconds (∼0.3 fields). The magenta line and dots in the second panel from top show median residuals for each field.

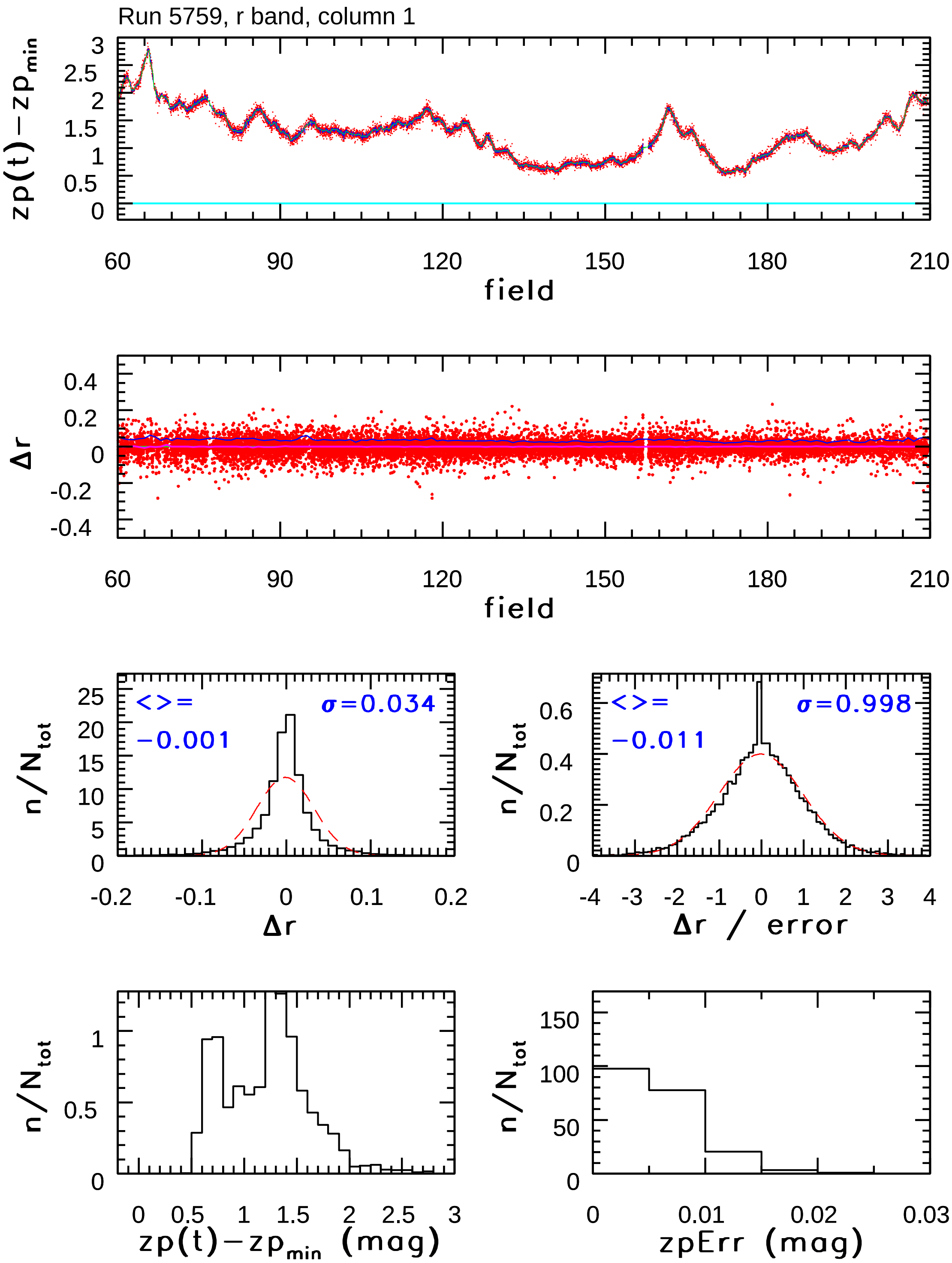

Fig. 16.— Analogous to Fig. 14, except that 1.5 hours worth of data from a run (5646) with moderately large cloud extinction is shown. Note that the median photometric zeropoint error is below 0.01 mag, although the median cloud extinction is larger than 1 mag.

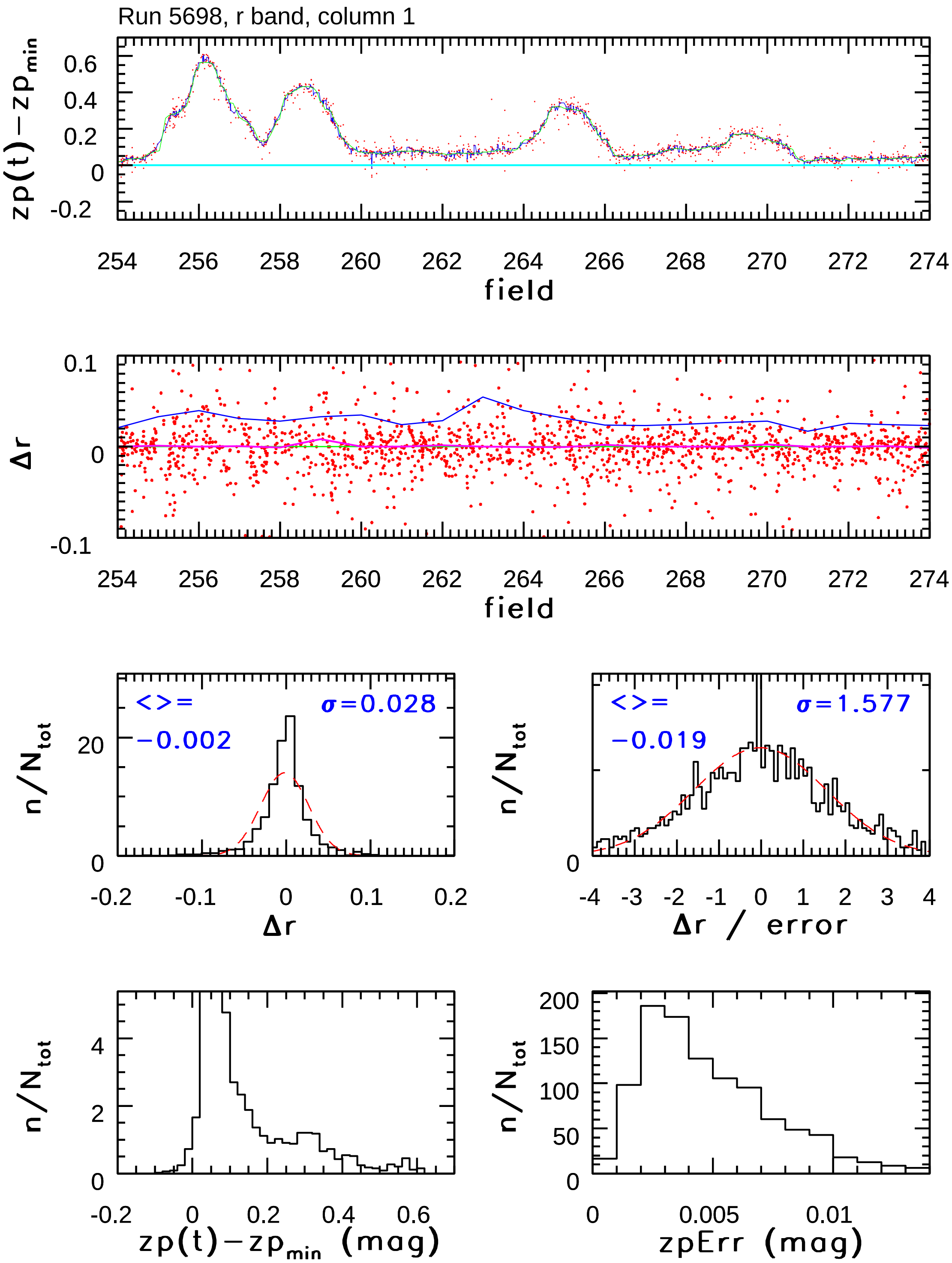

Fig. 17.— Analogous to Fig. 14, except that only 12 minutes worth of data from a run (5698) with relatively small cloud extinction is shown. Note that photometric zeropoint errors are well below 0.01 mag.

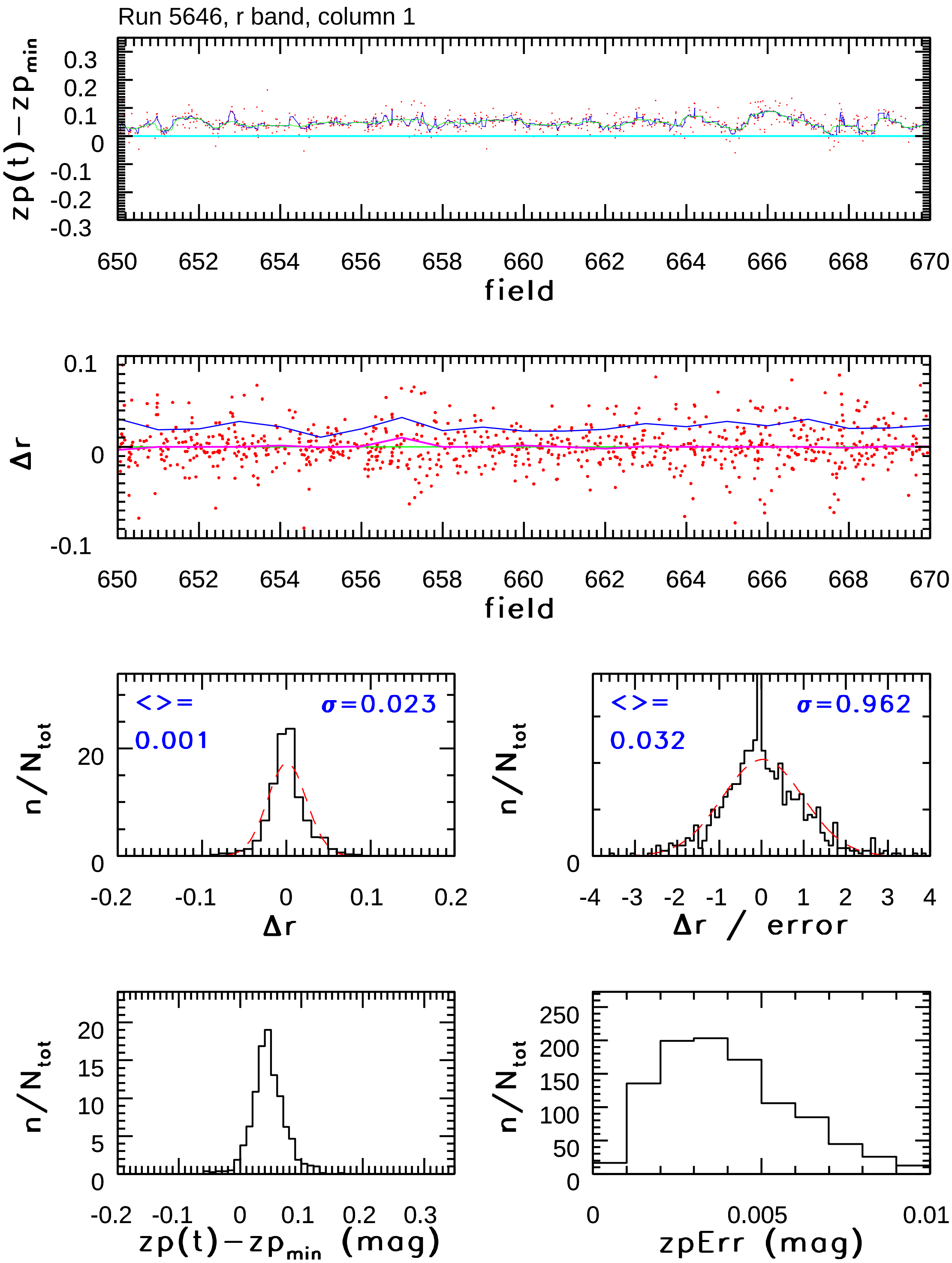

Fig. 18.— Analogous to Fig. 15, except that only 12 minutes worth of data with relatively small cloud extinction is shown.

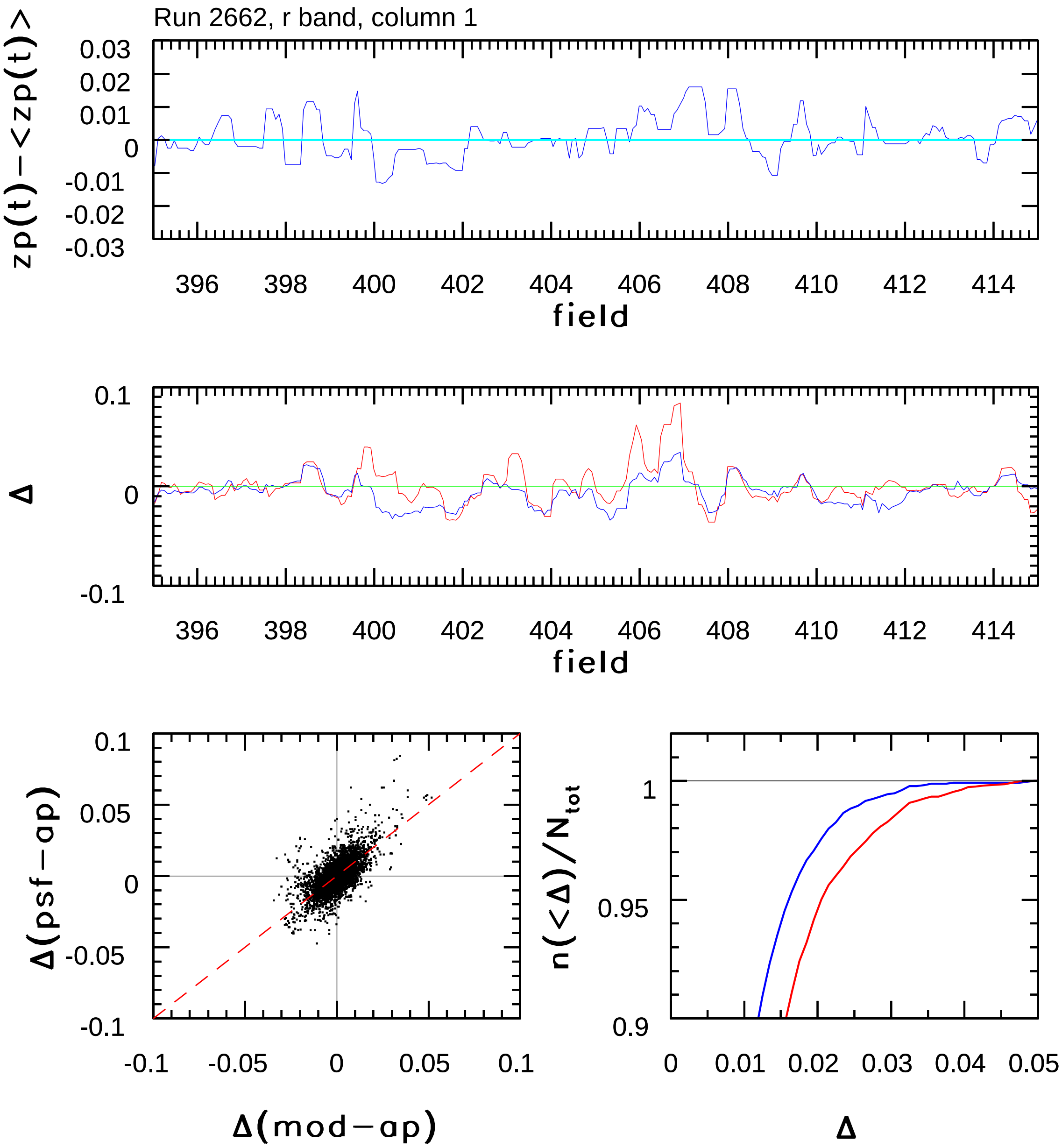

Fig. 19.— A comparison of calibration results using different types of magnitudes, for a stretch of data from SDSS-I run 2662. The top panel shows the variation of adopted zeropoint based on aperture magnitudes around its median for the displayed stretch. The middle panel shows the differences in the adopted zeropoints based on model (blue) and psf (red) magnitudes, and the zeropoints based on aperture magnitudes. The bottom left panel shows the correlation between these two zeropoint differences (psf-ap.mag and model-ap.mag), and the bottom right panel shows their normalized cumulative histograms. In fewer than 5% of cases does the disagreement between aperture and model magnitudes exceed 0.015 mag (0.02 mag for the aperture vs. psf magnitude difference), and the frequency of disagreements by more than 0.04 mag is about once in a thousand. The >0.04 mag disagreements are three times more likely for psf magnitudes.

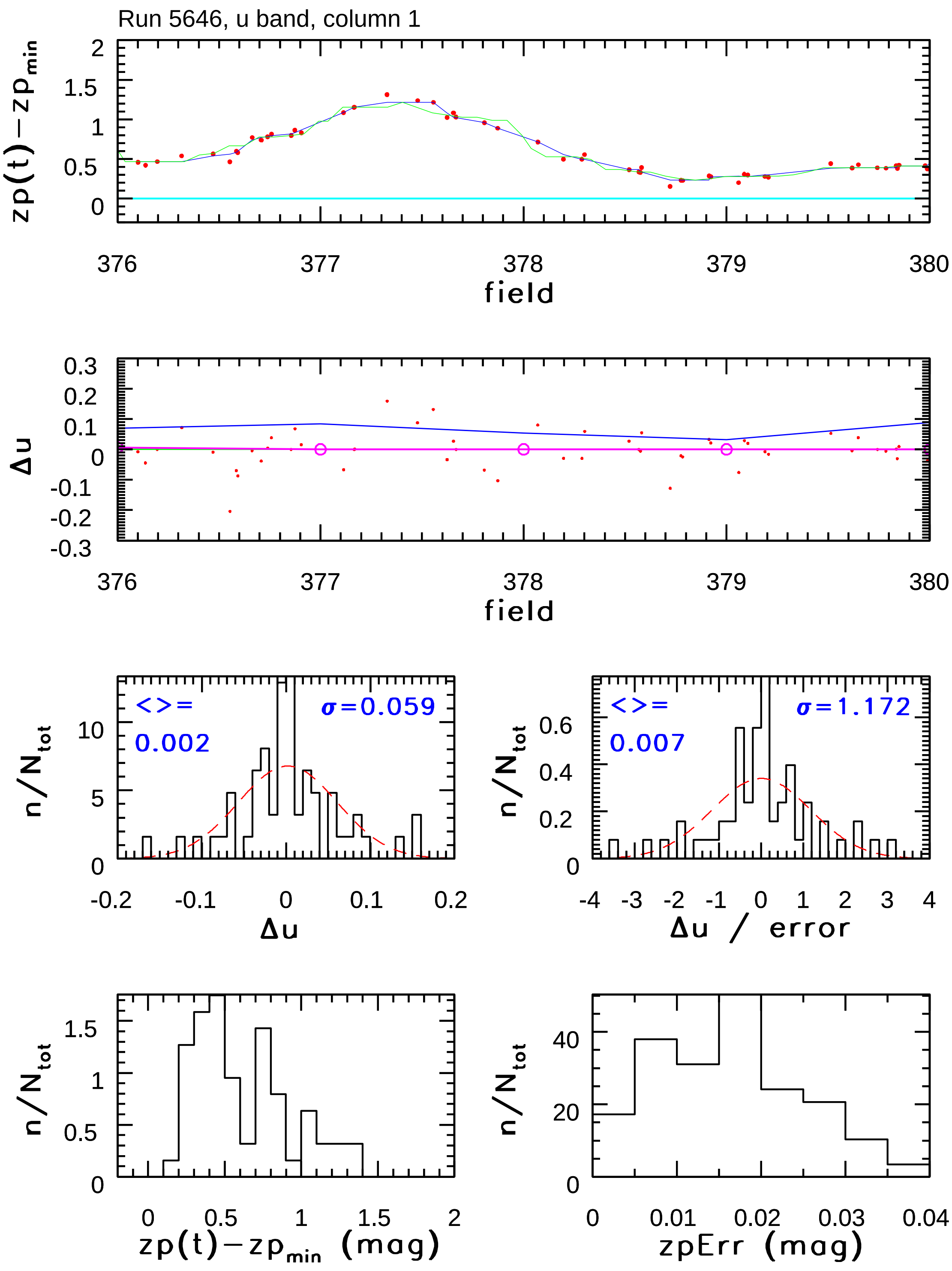

Fig. 20.— Analogous to Fig. 15, except that the u band calibration summary is shown. Note the much smaller number of calibration stars than in redder bands. Nevertheless, it is still possible to photometrically calibrate these data with the median calibration error of 0.02 mag.

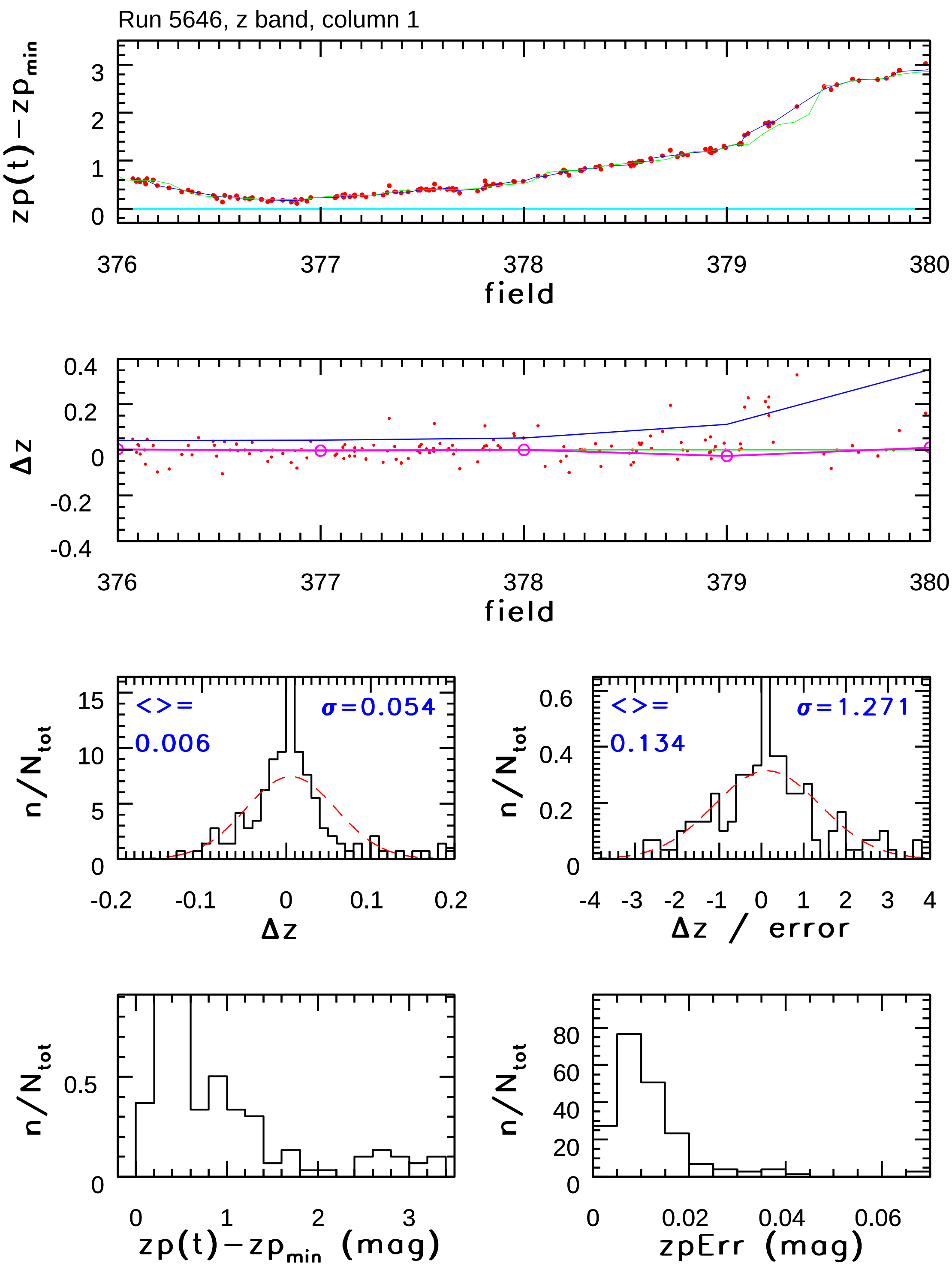

Fig. 21.— Analogous to Fig. 20, except that the z band calibration summary is shown.

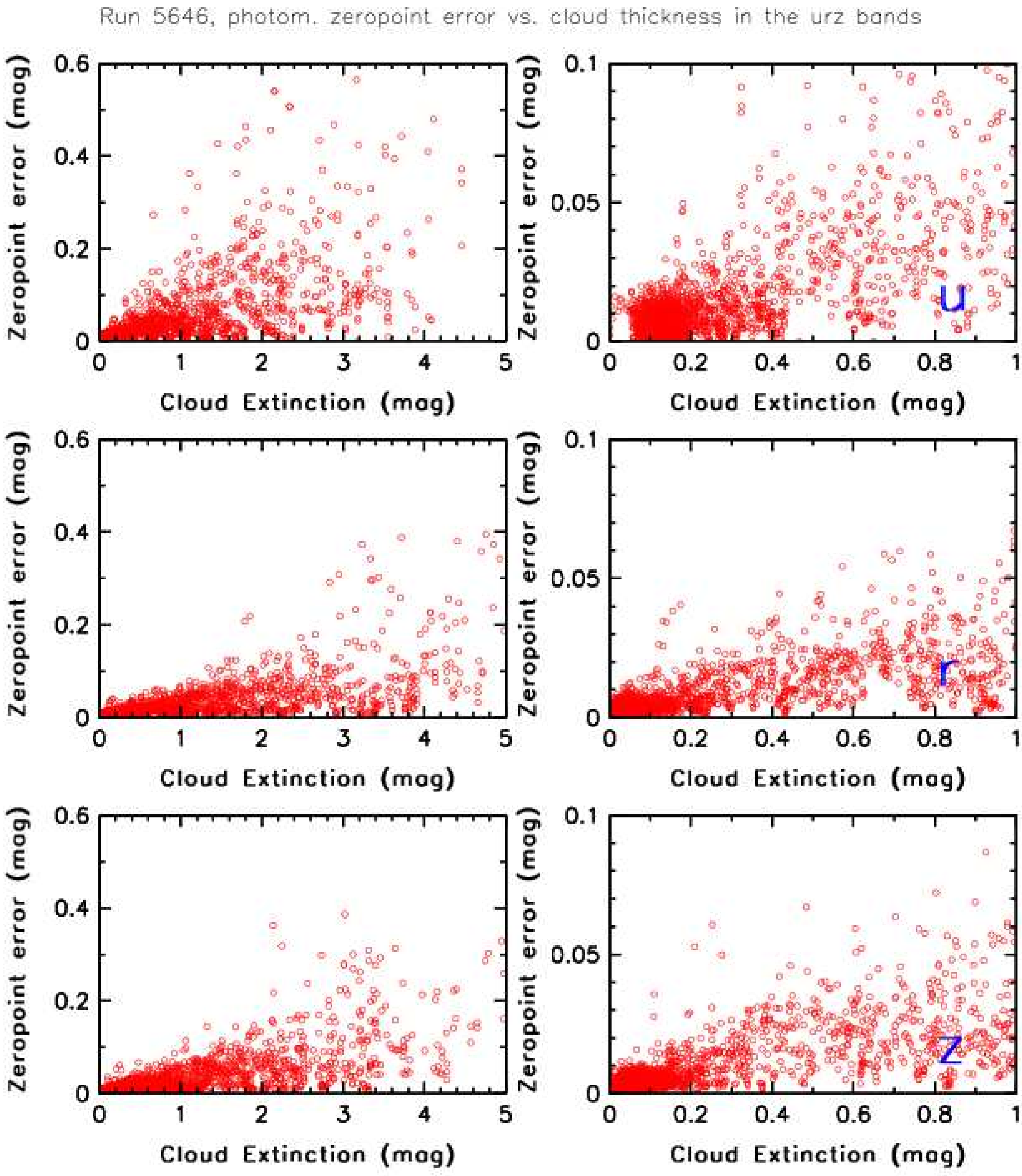

Fig. 22.— An illustration of calibration accuracy as a function of the cloud extinction and band (urz as marked in the panels). Each symbol represents one calibration patch (a ∼5 arcmin^2 large rectangle with 1:20 aspect ratio). Zeropoint error is determined from the root-mean-scatter of photometric residuals. The panels in the right column are zoomed in versions of those in the left column. Note that the data can be calibrated with zeropoint errors typically smaller than 0.05 mag even through 1 mag thick clouds.

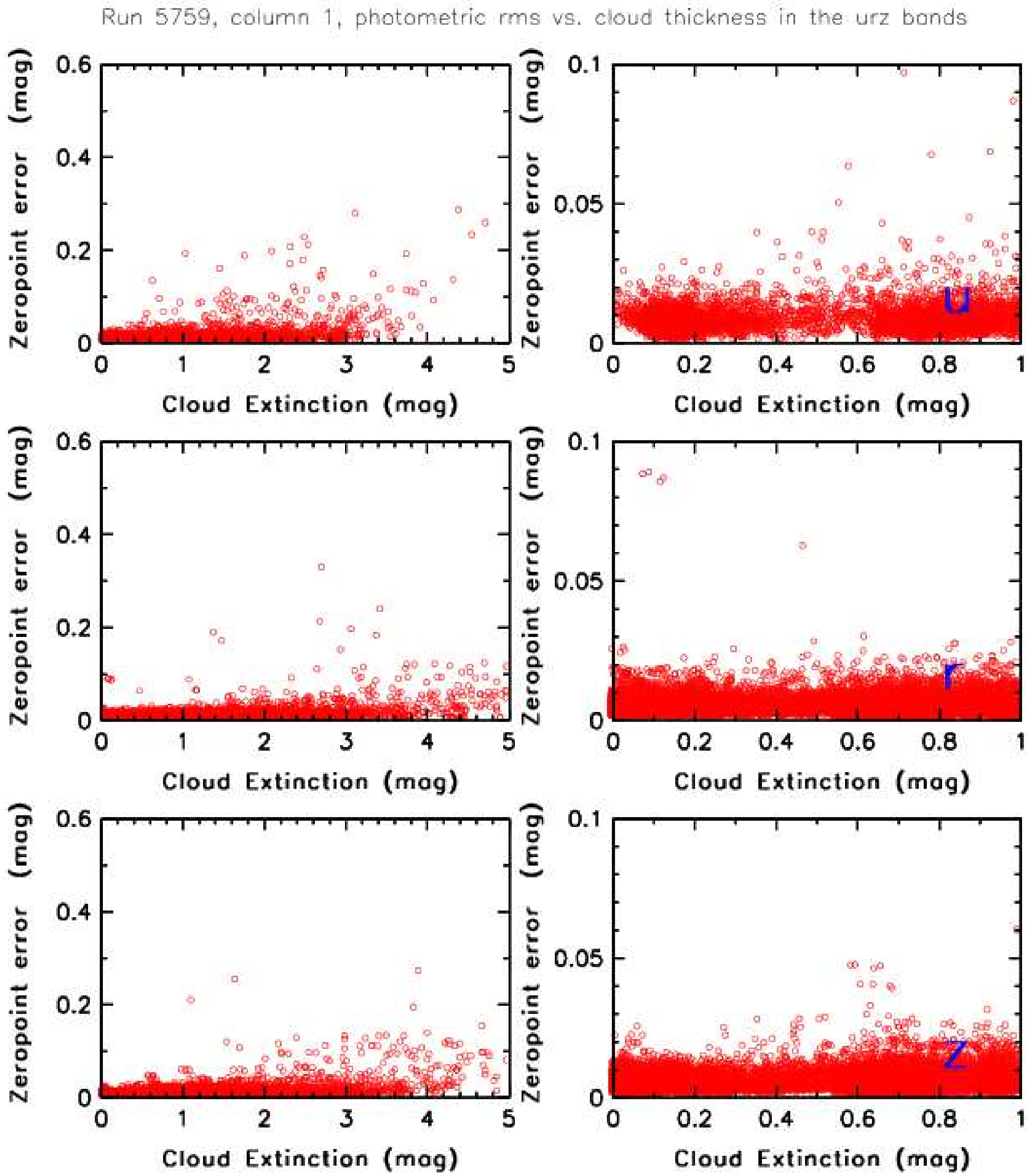

Fig. 23.— Analogous to Figure 22, except for a run (5759) with much less cloud structure. The data can be calibrated with zeropoint errors typically smaller than 0.02 mag even through 1 mag thick clouds.

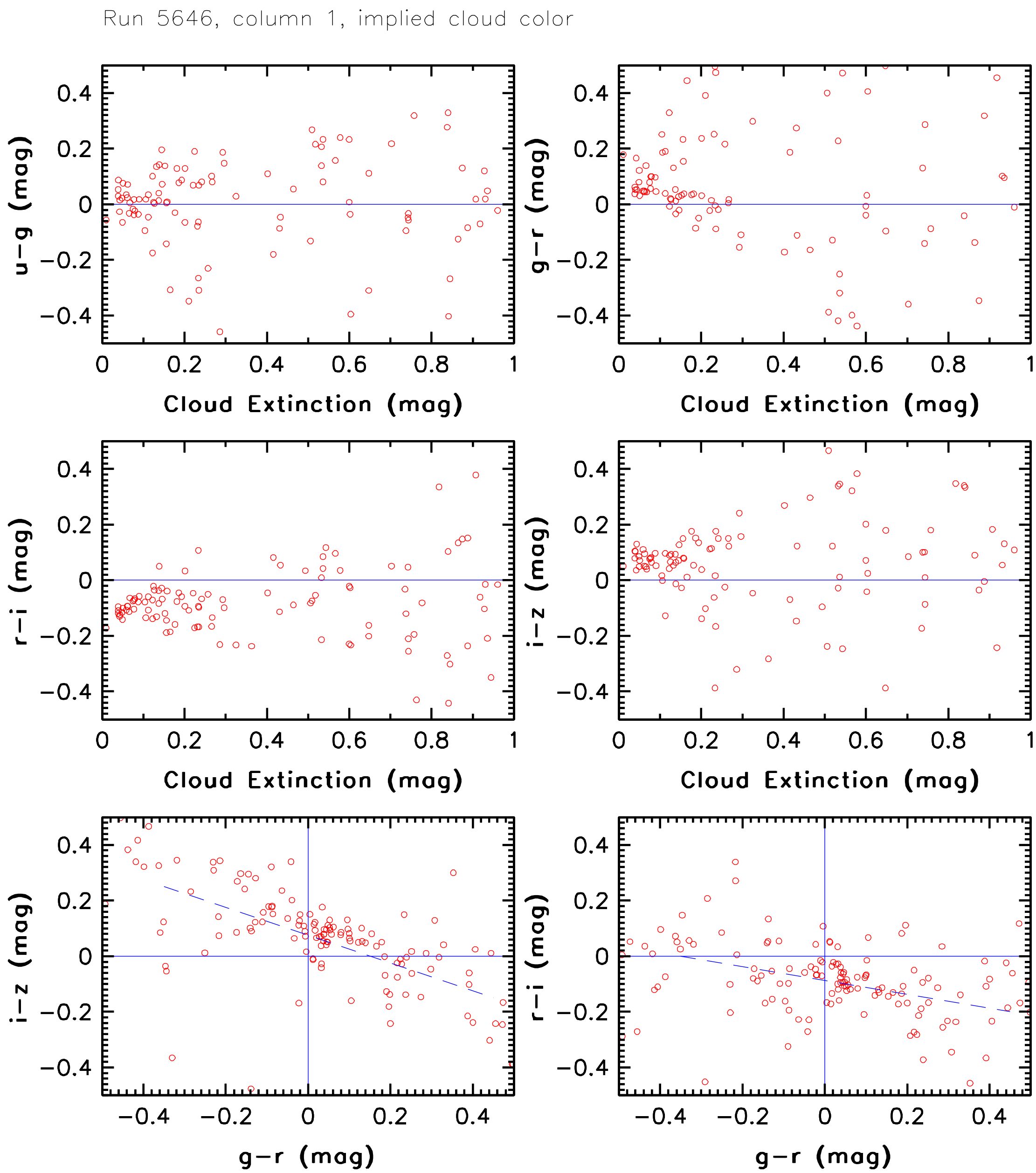

Fig. 24.— The color of cloud extinction in SDSS bands. Each symbol represents one field. The dashed lines in the bottom two panels indicate expected correlation if the color variations are due to temporal changes in the cloud thickness (rather than due to intrinsic color changes).

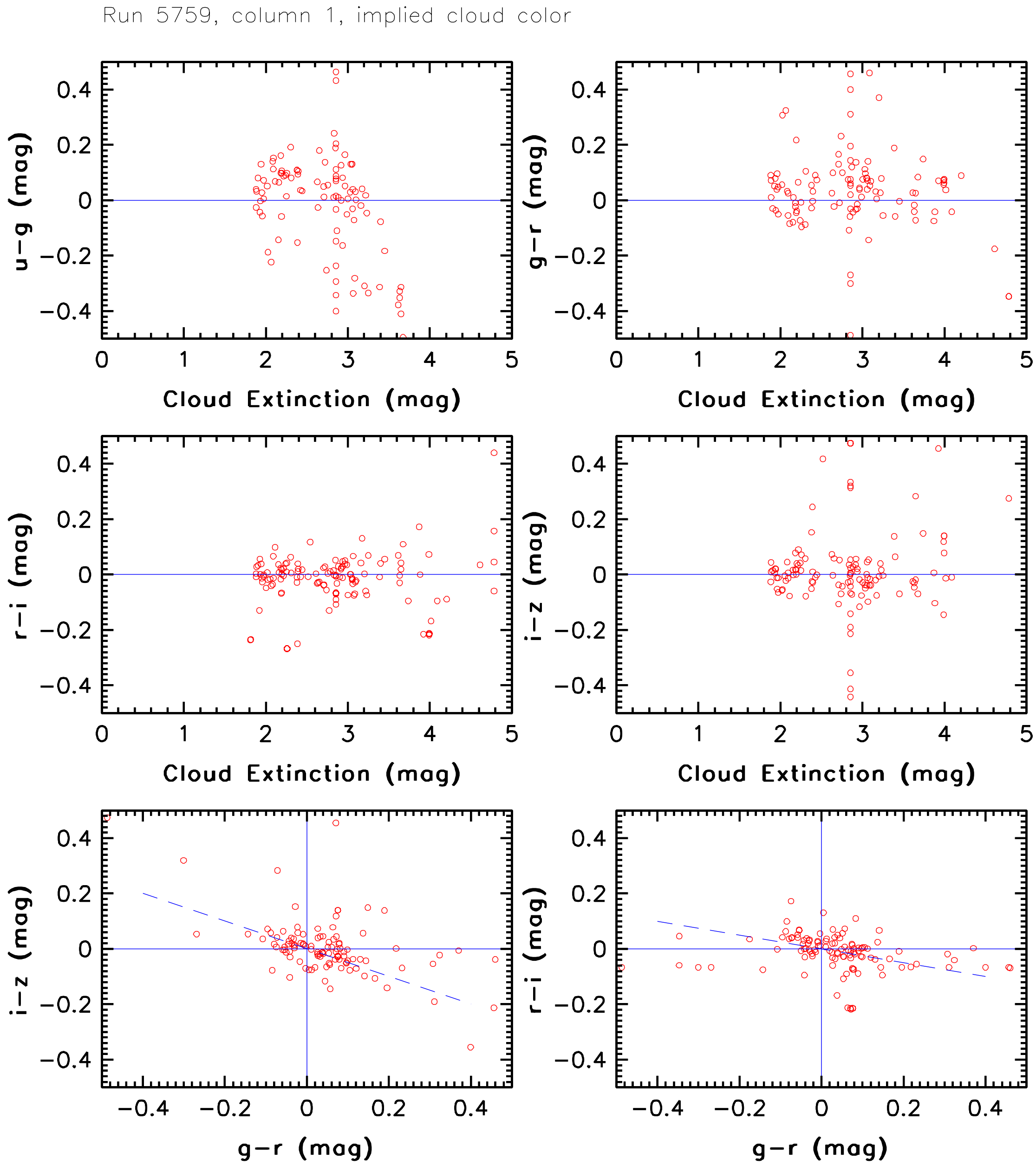

Fig. 25.— Analogous to Figure 24, except for a run (5759) with much less cloud structure.

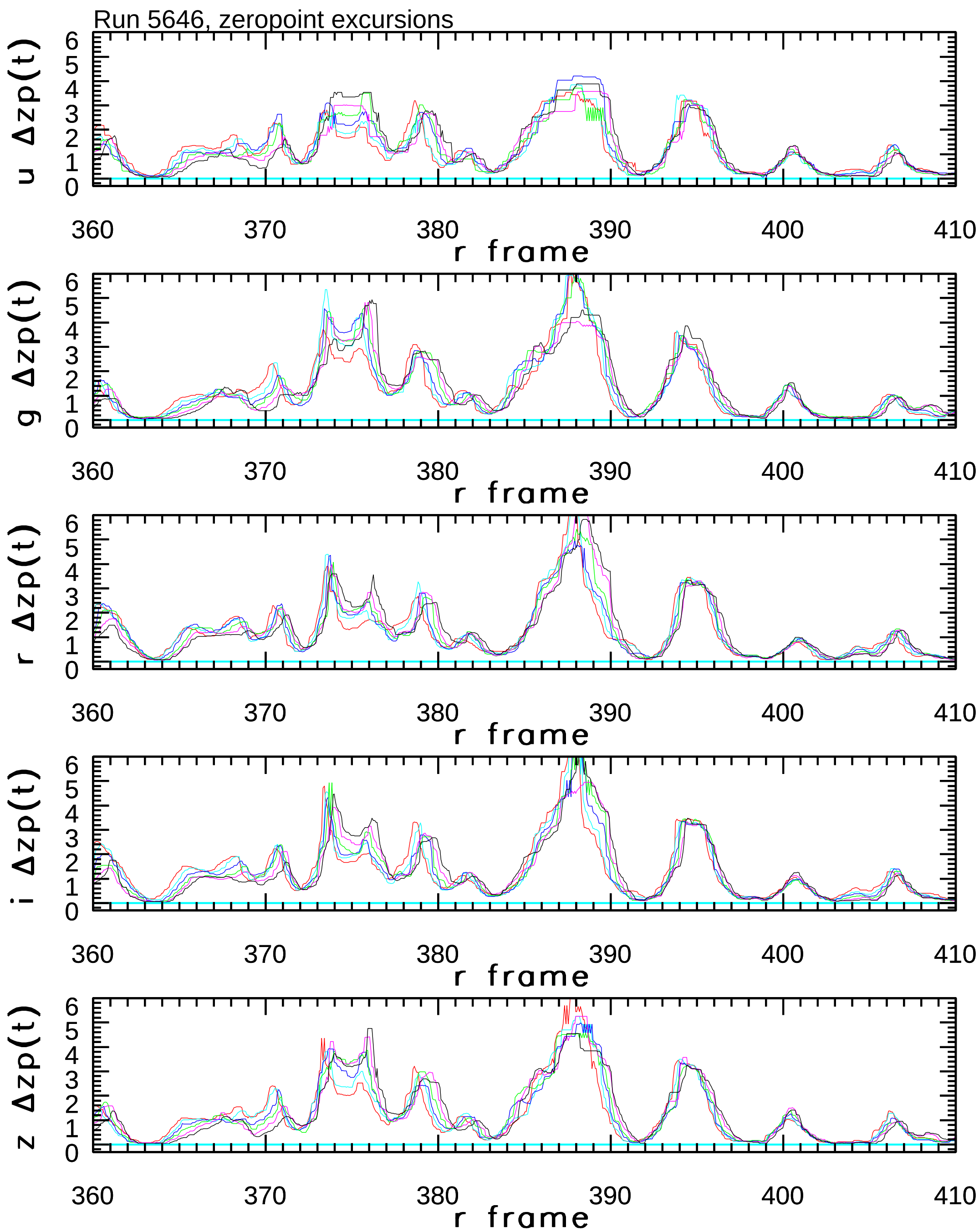

Fig. 26.— A comparison of cloud extinction measured for six camera columns and in five different bands during about half an hour of scanning. In each panel, six lines correspond to six camera columns. While overall behavior is similar, cloud extinction can vary by more than 1 mag across the camera (∼2.5 degree).

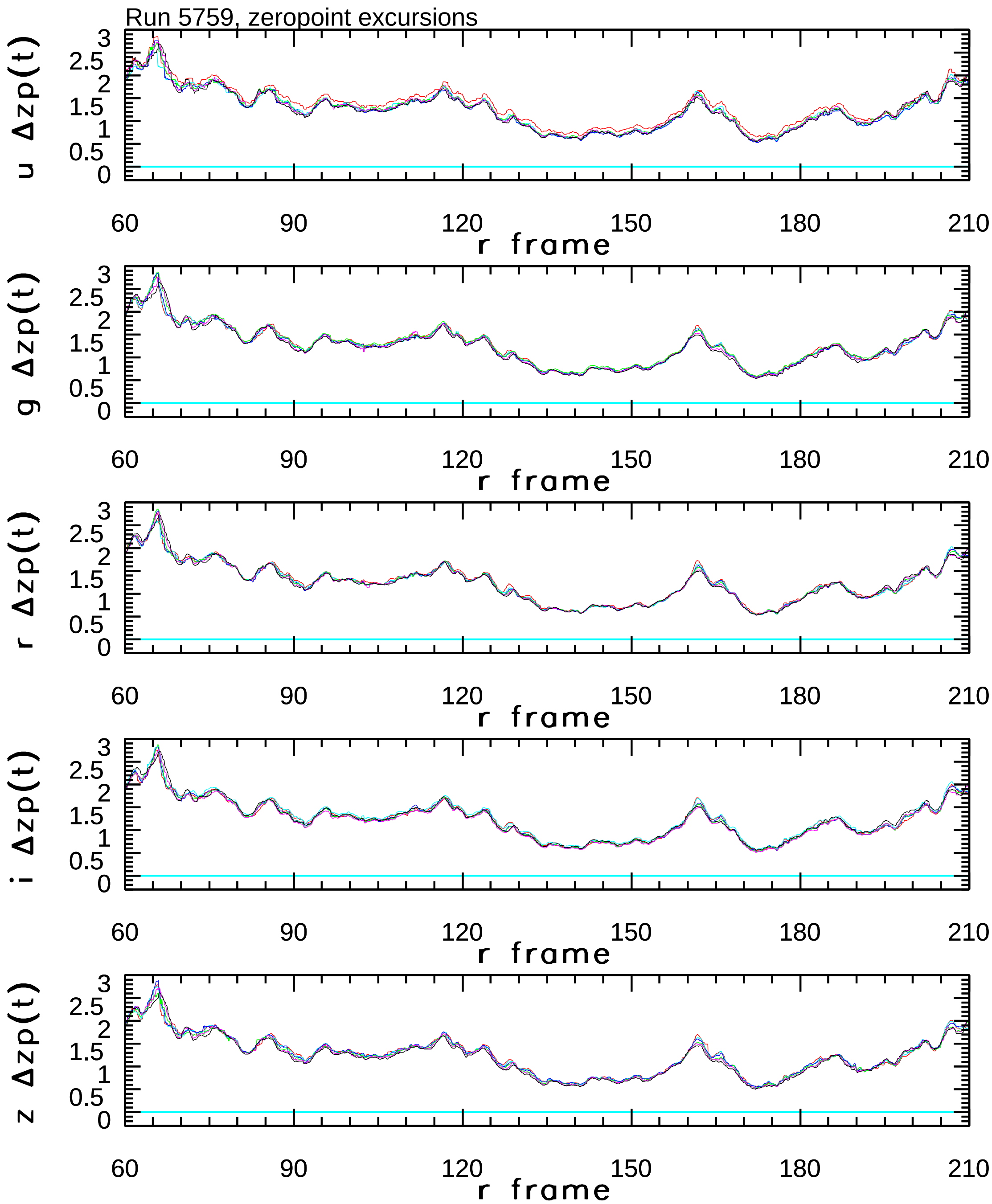

Fig. 27.— Analogous to Figure 26, except that a run with exceptionally "smooth" clouds is shown (5759). Note much smaller differences between the zeropoints for different columns than in Figure 26.

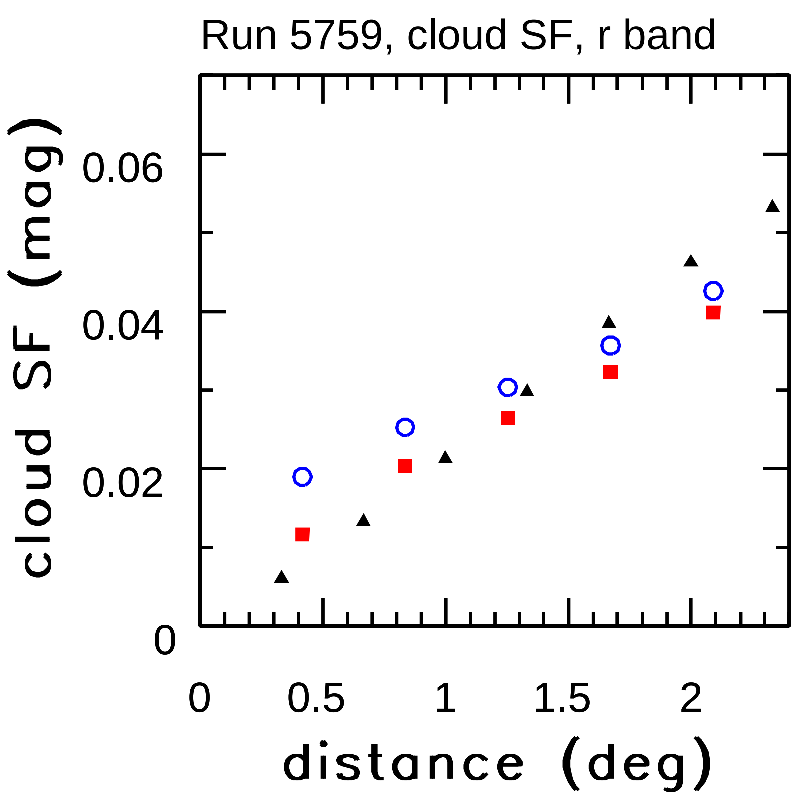

Fig. 28.— The cloud structure function in the r band for run 5759. The circles show the width of the distribution of zeropoint differences between camera column 1 and other columns. This width is corrected for 0.015 mag contribution from the measurement errors and shown by squares. The triangles show the width of the distribution of zeropoint differences in the in-scan direction, with the distance scale multiplied by 30. This multiplication factor measures the cloud speed relative to the boresight in the in-scan direction (see text).

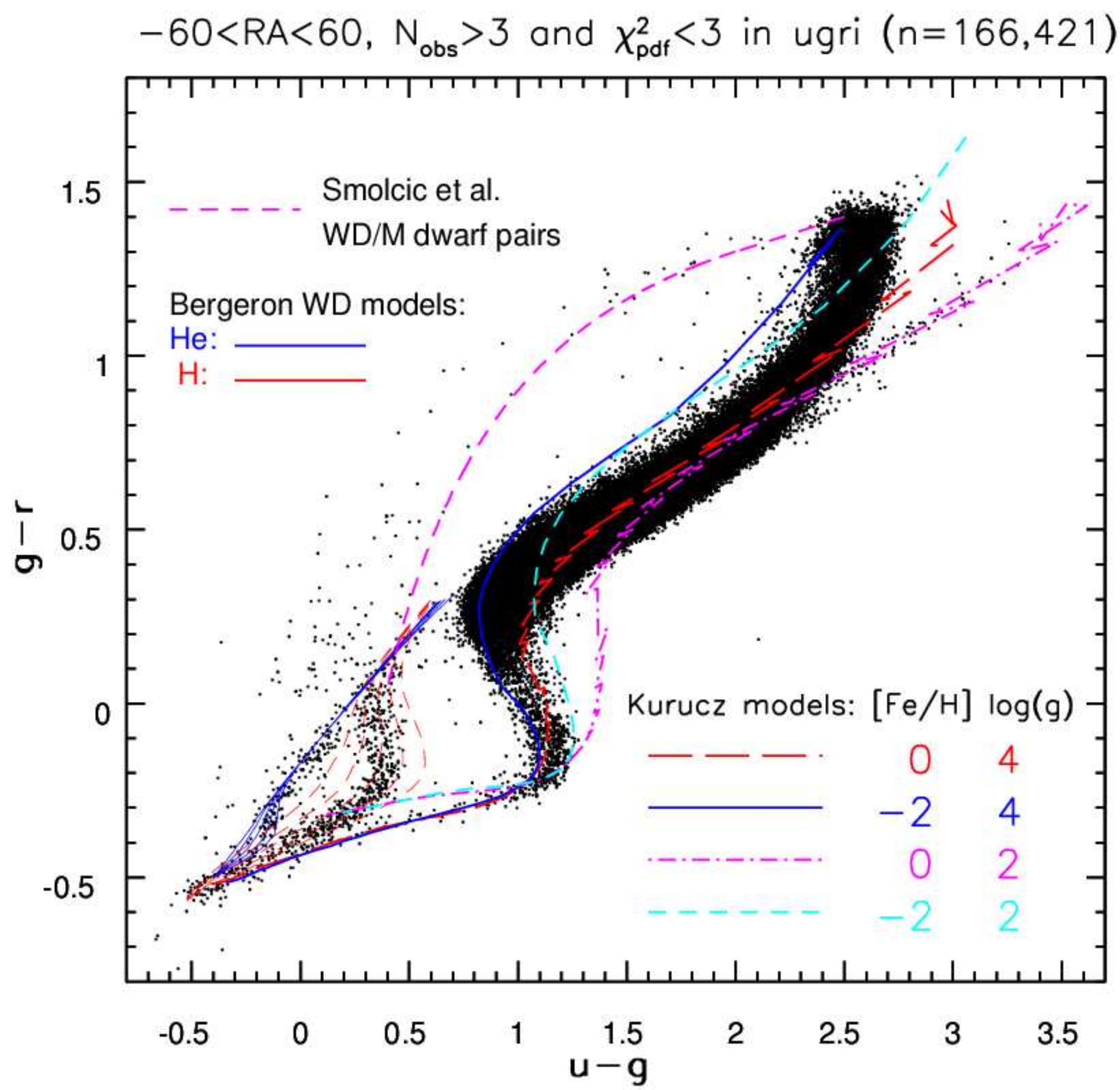

Fig. 29.— The $g - r$ vs. $u - g$ color-color diagrams for all non-variable point sources constructed with the improved averaged photometry (dots). The various models are shown by lines, as marked in the figure.

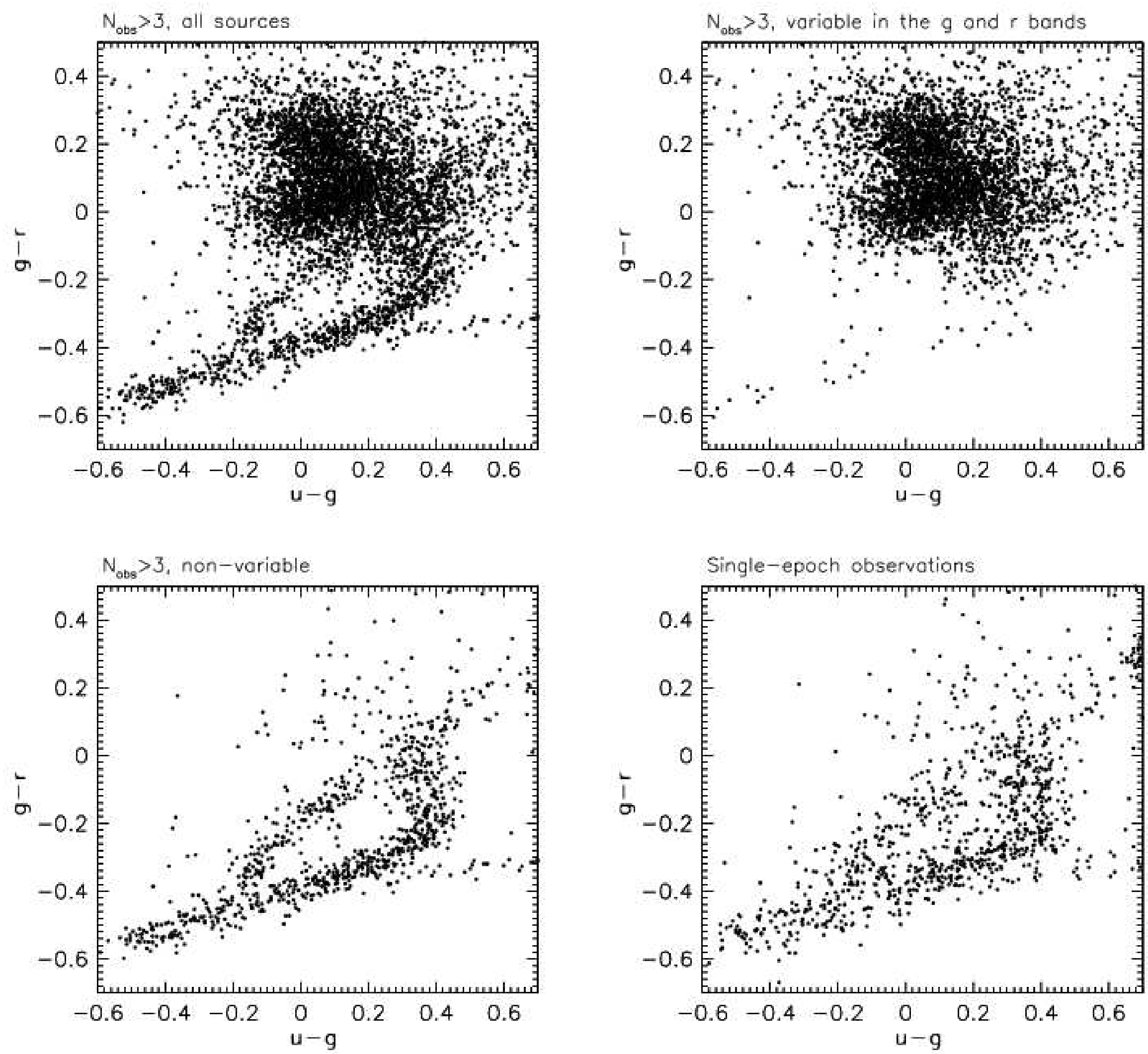

Fig. 30.— The top left panel shows the blue region of the $g - r$ vs. $u - g$ diagram for *all* sources with the averaged photometry. The top right panel shows *only* the variable sources, and the bottom left panel shows the non-variable sources. The bottom right panel shows the *same* non-variable sources, but using their DR5 single-epoch photometry. Note the striking difference between the two bottom panels.